Imaging of the pial arterial vasculature of the human brain *in vivo* using high-resolution 7T time-of-flight angiography

Saskia Bollmann[1,2,3], Hendrik Mattern[4], Michaël Bernier[1,2], Simon D. Robinson[3,5,6,7], Daniel Park[1], Oliver Speck[4,8,9,10], Jonathan R. Polimeni[1,2,11]

[1]Athinoula A. Martinos Center for Biomedical Imaging, Massachusetts General Hospital, Charlestown, MA, USA

[2]Department of Radiology, Harvard Medical School, Boston, MA, USA

[3]Centre for Advanced Imaging, The University of Queensland, Brisbane, QLD, Australia

[4]Department of Biomedical Magnetic Resonance, Institute of Experimental Physics, Otto-von-Guericke-University, Magdeburg, Germany

[5]High Field MR Centre, Department of Biomedical Imaging and Image-guided Therapy, Medical University of Vienna, Vienna, Austria

[6]Karl Landsteiner Institute for Clinical Molecular MR in Musculoskeletal Imaging, Vienna, Austria

[7]Department of Neurology, Medical University of Graz, Graz, Austria

[8]German Center for Neurodegenerative Diseases, Magdeburg, Germany

[9]Center for Behavioral Brain Sciences, Magdeburg, Germany

[10]Leibniz Institute for Neurobiology, Magdeburg, Germany

[11]Division of Health Sciences and Technology, Massachusetts Institute of Technology, Cambridge, MA, USA

Abstract

The pial arterial vasculature of the human brain is the only blood supply to the neocortex, but quantitative data on the morphology and topology of these mesoscopic arteries (diameter 50–300 µm) remains scarce. Because it is commonly assumed that blood flow velocities in these vessels are prohibitively slow, non-invasive time-of-flight MRI angiography (TOF-MRA)—which is well-suited to high 3D imaging resolutions—has not been applied to imaging the pial arteries. Here, we provide a theoretical framework that outlines how TOF-MRA can visualize small pial arteries *in vivo*, by employing extremely small voxels at the size of individual vessels. We then provide evidence for this theory by imaging the pial arteries at 140-µm isotropic resolution using a 7T MRI scanner and prospective motion correction, and show that pial arteries one voxel-width in diameter can be detected. We conclude that imaging pial arteries is not limited by slow blood flow, but instead by achievable image resolution. This study represents the first targeted, comprehensive account of imaging pial arteries *in vivo* in the human brain. This ultra-high-resolution angiography will enable the characterization of pial vascular anatomy across the brain to investigate patterns of blood supply and relationships between vascular and functional architecture.

Contents

Abstract 2

Introduction 5

Theory 8

Anatomical architecture of the pial arterial vasculature 8

Flow-related enhancement 10

Introducing a partial-volume model 14

Inflow-artefacts in sinuses and pial veins 15

Velocity- and TE-dependent vessel displacement artifacts 16

Considerations for imaging the pial arterial vasculature 16

Results 18

Effect of voxel size on flow-related enhancement 18

Imaging the pial arterial vasculature 19

Vessel displacement artefacts 21

Removal of pial veins 22

Discussion 23

A new perspective on imaging the pial arterial vasculature 23

Extending classical FRE treatments to the pial vasculature 23

Imaging limitations 24

Challenges for vessel segmentation algorithms 28

Future directions 31

Methods 33

Simulations 33

Data acquisition 33

Data analysis 35

Supplementary material 37

Estimation of vessel-volume fraction 37

Effect of FRE Definition and Interaction with Partial-Volume Model 38

Optimization of repetition time and excitation flip angle 39

Imaging of the pial arterial vasculature 41

Increase in skeleton length 45

Vessel displacement artefact 45

Potential for advanced segmentations algorithms 47

Acknowledgements 48

References 49

Introduction

The pial arterial vasculature of the cerebrum consists of smaller distal arteries and arterioles that cover the cerebral cortical surface, and connects the branches of the three major supplying arteries of the cerebrum—the anterior, middle and posterior cerebral arteries—with the penetrating intracortical arterioles, which deliver blood into the cortical grey matter (Cipolla, 2009; Jones, 1970). Notably, the pial arterial vasculature is the only source of blood supply to the neocortex (Mchedlishvili and Kuridze, 1984), and its redundancies are organized in three tiers: global re-routing of blood through the circle of Willis, intermediate anastomoses between branches originating from the three major arteries, and local loops formed by pial anastomoses within the same branch (Blinder et al., 2010; Duvernoy et al., 1981).

Although extensive anatomical studies have described topological properties and the relevant constituents of the pial arterial vasculature (Pfeifer, 1930; Szikla et al., 1977), *quantitative* data of the human pial arterial vasculature remain scarce (Cassot et al., 2006; Helthuis et al., 2019; Hirsch et al., 2012; Payne, 2017; Schmid et al., 2019). The by far still 'most comprehensive and influential work' (Hirsch et al., 2012) is the detailed description of the pial vasculature by Duvernoy et al. (1981), which examined 25 brains using intravascular ink injections. As indispensable as this dataset has been, 3D reconstructions of the vascular network and surrounding anatomy were not provided in this study. A second recent analysis performed by Helthuis et al. (2019) used corrosion casts from four brain specimens and provided valuable insights into the branching pattern of the arterial vasculature. However, only limited information can be obtained in this way about the morphometry of vessels, in particular their position and geometric relationship with the cortex. Further, the elaborate preparation and the limitation to *ex vivo* samples restricts the applicability of these methods when, for example, one wants to characterize the large variability across individuals in pial arterial morphometry (Alpers et al., 1959; Beevor and Ferrier, 1909; Cilliers and Page, 2017; Gomes et al., 1986; Papantchev et al., 2013; Stefani et al., 2000; van der Zwan et al., 1993) and function (Baumbach and Heistad, 1985; van Laar et al., 2006).

Given the central role of the pial arterial vasculature for healthy human brain function (Hirsch et al., 2012; Iliff et al., 2013; Xie et al., 2013), its impact on functional magnetic resonance imaging (fMRI) signals (Bright et al., 2020; Chen et al., 2020), and its involvement in numerous cerebrovascular diseases (Hetts et al., 2017; McConnell et al., 2016), there is a clear need to be able to image the pial arterial vasculature in individual subjects to characterize its morphometry and topology including arterial diameter and geometric relationship with the cortex (Mut et al., 2014). For example, many intracranial pathologies have selective involvement of superficial vessels (Ginat et al., 2013; Herz et al., 1975; Hetts et al., 2017; McConnell et al., 2016; Song et al., 2010; Uhl et al., 2003), and the outcome

of stroke patients is heavily dependent on the status of the collateral circulation (Ginsberg, 2018; Raymond and Schaefer, 2017). Yet existing hemodynamic modeling approaches have to synthesize the pial arterial vasculature either implicitly (Park et al., 2020) or explicitly (Ii et al., 2020) from an incomplete quantitative understanding of its morphometry and variability. In addition, modelling of hemodynamic changes in response to neural activity needs to account for the effect of pial vessels (Markuerkiaga et al., 2016; Polimeni et al., 2010; Uludağ and Blinder, 2018). Although signal changes in fMRI data using a blood-oxygenation-level-dependent (BOLD) contrast arise predominantly on the venous side of the vascular hierarchy (Ogawa et al., 1990), the strongest *vascular* response to neural activity is located in intracortical arteries and arterioles (Hillman et al., 2007; Vanzetta, 2005), and significant diameter changes in upstream arteries have been observed (Bizeau et al., 2018; Cho et al., 2012, 2008). With the recent interest in cerebral blood volume-based fMRI (Huber et al., 2014) and the numerous accounts of vascular contributions found in BOLD fMRI signals (Amemiya et al., 2020; Bright et al., 2020; Chen et al., 2020; Drew et al., 2020), including a detailed, subject-specific depiction of the underlying angio-architecture would immensely augment forthcoming modelling initiatives (Havlicek and Uludağ, 2020; Tak et al., 2014).

So far, numerous approaches exist to image large, *macro*scopic proximal intracranial arteries such as the circle of Willis including its branches and the basal arteries with magnetic resonance imaging (MRI) (Carr and Carroll, 2012). Similarly, the density of *micro*scopic, parenchymal vessels can be quantified through techniques such as vessel size imaging and capillary density imaging (Kiselev et al., 2005; Troprès et al., 2001; Xu et al., 2011), and newer methods for estimates of cerebral blood volume of the arteriolar side of the microvascular tree (Hua et al., 2019). However, direct non-invasive imaging of the *meso*scopic vessels of the pial arterial network, i.e. arteries with a diameter between 50 and 300 µm, is not in current use, either in clinical practice or in basic research.

Recent studies have shown the potential of time-of-flight (TOF) based magnetic resonance angiography (MRA) at 7 Tesla (T) in subcortical areas (Bouvy et al., 2016, 2014; Ladd, 2007; Mattern et al., 2018; Schulz et al., 2016; von Morze et al., 2007). In brief, TOF-MRA uses the high signal intensity caused by inflowing water protons in the blood to generate contrast, rather than an exogenous contrast agent. By adjusting the imaging parameters of a gradient-recalled echo (GRE) sequence, namely the repetition time (T_R) and flip angle, the signal from static tissue in the background can be suppressed, and high image intensities are only present in blood vessels freshly filled with non-saturated inflowing blood. As the blood flows through the vasculature within the imaging volume, its signal intensity slowly decreases. (For a comprehensive introduction to the principles of MRA, see for example Carr and Carroll (2012). At ultra-high field, the increased signal-to-noise ratio (SNR), the longer T_1 relaxation times of blood and grey matter, and the potential for higher resolution are key

benefits (von Morze et al., 2007). However, the current description of the MR physics underlying TOF-MRA (Brown et al., 2014a; Carr and Carroll, 2012) is not tailored to imaging pial arteries, because their small diameter and complex branching pattern require particular considerations. For example, while the advantage of reduced voxel size for imaging small arteries has empirically been shown numerous times (Haacke et al., 1990; Mattern et al., 2018; von Morze et al., 2007), the sentiment prevails (Chen et al., 2018; Masaryk et al., 1989; Mut et al., 2014; Park et al., 2020; Parker et al., 1991; Wilms et al., 2001; Wright et al., 2013) that the slower flow in small arteries should significantly diminish the TOF effect (Haacke et al., 1990; Pipe, 2001), and perhaps for that reason imaging the pial arterial vasculature *in vivo* has received little attention. Here, we revisit the topic of high-resolution TOF-MRA to investigate the feasibility of imaging the pial arterial vasculature *in vivo* at 7T. We demonstrate, based on simulations and empirical data, that pial arteries can be detected reliably. Note that while some, particularly larger pial arterials, have undoubtedly been visualized incidentally in high resolution images, we present here the first targeted, comprehensive account of imaging the pial arteries.

In the following, we first summarize the relevant properties of the pial arterial vasculature, in particular vessel diameter, blood velocity and blood delivery time. With this in mind, we revisit the theory behind 3D TOF-MRA and derive optimal parameters for imaging these vessels. We then demonstrate the supra-linear relationship between vessel contrast and voxel size and explore the requirements for accurate vessel detection. This work argues that, from a physiological and theoretical perspective, it is indeed possible to image the pial arterial network using a TOF-based contrast. Subsequently, we present results from several experiments supporting our hypothesis and ultimately employ high-resolution TOF-MRA with prospective motion correction to image the pial arterial vasculature at 140 µm isotropic resolution.

Theory

Anatomical architecture of the pial arterial vasculature

The pial arterial vasculature consists of smaller arteries and arterioles on the cortical surface (Figure 1, left) (Duvernoy, 1999). Pial arteries range in diameter from 280 µm to 50 µm and connect to the smaller (< 50 µm) intracortical arterioles. Similar values of 700 µm to 30 µm in pial arterial diameter were also reported by Nonaka et al. (2003b), who exclusively characterized the calcarine fissure. The recent work on the topology of the vascular system by Hirsch et al. (2012) might create the impression that mesoscopic pial vessels entirely cover the cortical surface (e.g. Figure 2 in Hirsch et al. (2012)). However, the segmentation provided by Duvernoy (1999) shows that pial cerebral blood vessels are rather sparse, and only approximately 17 % of the human cortex is covered by arteries, and 11 % by veins[1]. Pial arteries exhibit a distinctive branching pattern on the cortical surface, in that an arterial branch arises at a nearly right angle from its parent vessel (Rowbotham and Little, 1965), usually with a significantly reduced diameter. In the absence of ground-truth data, this conspicuous feature constitutes an important prior that can be used as an image quality marker: simply, the more right-angled branches are detected, the higher the sensitivity to small arteries.

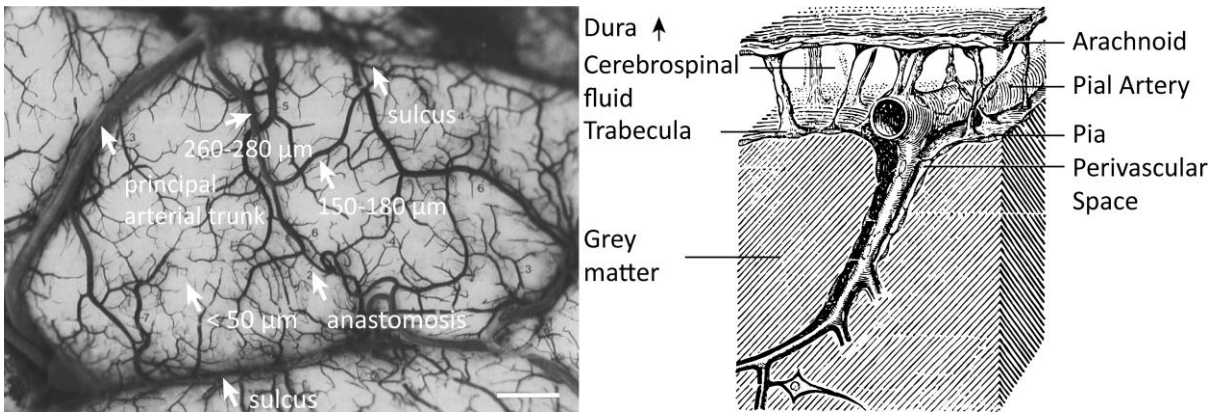

Figure 1: LEFT: The pial vascular network on the medial orbital gyrus depicted using intravascular india ink injection (adapted with permission from Duvernoy (1999)). The arrows indicate the average diameter of central pial arteries (260 – 280 µm), peripheral pial arteries (150 – 180 µm), and pial arterioles (< 50 µm). Pial anastomoses are commonly formed by arteries ranging from 25 µm to 90 µm in diameter. For reference, the diameter of intracortical penetrating arterioles is approximately 40 µm (scale bar: 2.3 mm). RIGHT: Pia-arachnoid architecture (adapted with permission from Ranson and Clark (1959)) illustrates the complex embedding of pial vessels, which are surrounded by various membrane layers that form the blood-brain barrier, cerebrospinal fluid and grey matter (Marín-Padilla, 2012; Mastorakos and McGavern, 2019; Ranson and Clark, 1959).

From a cross-sectional point of view cutting through the cortex, pial arteries are embedded in the meningeal layers between the pia and arachnoid mater, i.e. the subarachnoid space (Figure 1, right). Thus, their immediately surrounding tissue is not only grey matter, but a mixture of grey matter,

[1] To obtain a rough estimate of their density, we segmented the stylized drawing accompanying Figure 1 (Duvernoy, 1999); see also subsection *Data analysis* below.

cerebrospinal and interstitial fluid, and meningeal and glial tissue (Marín-Padilla, 2012). In the next section, we will propose a simplified partial-volume model to account for the small diameter of pial arteries. Nevertheless, one should keep in mind that the actual surrounding of pial arteries consists of a number of different tissue classes and fluids, with considerable differences in T_1 values, especially between grey matter, arterial blood, and cerebrospinal fluid (Rooney et al., 2007; Wright et al., 2008).

Along with their diameter, the blood velocity within pial arteries is an important factor determining the TOF contrast. However, blood velocity values in human pial arteries are difficult to obtain due to their small size. Using optical imaging in cats, Kobari et al. (1984) measured blood velocities in pial arteries ranging from 20 µm to 200 µm diameter. For example, in pial arteries with a diameter between 100 µm and 150 µm, the centerline velocity was 42.1 mm/s. Similar values were obtained by Nagaoka and Yoshida (2006) for arterioles in the human retina using laser Doppler velocimetry, where the average centerline velocity for first-order arterioles with an average diameter of 107.9 µm was 41.1 mm/s. The only study in humans measuring blood velocity in small cerebral arteries was performed by Bouvy et al. (2016) using quantitative flow MRI. They estimated mean blood velocities of 39 mm/s to 51 mm/s in the basal ganglia, where arterial diameters range from 175 µm to 668 µm (Djulejić et al., 2015). Figure 2 provides a comprehensive overview of all blood velocity values and vessel diameters reported for pial arteries. Note that optical imaging methods (Kobari et al., 1984; Nagaoka and Yoshida, 2006) are expected to considerably overestimate the mean velocity within the vessel, whereas MRI-based measurements can severely underestimate the velocity values due to partial volume effects (Bouvy et al., 2016; Hofman et al., 1995; Tang et al., 1993). This might explain the large discrepancies that are apparent in Figure 2 between optical and MRI based methods. Due to the gradual reduction in vessel diameter along the vascular tree, the reported velocity values only apply to the very last branch, and faster velocities are expected along much of the vasculature. For example, blood velocities in the three major cerebral arteries exceed the velocity values depicted here by at least an order of magnitude (Lee et al., 1997; Molinari et al., 2006).

The *blood delivery time* for a given voxel containing a vessel is the time it takes for the blood water spins to reach that voxel after they first enter the imaging slab, and is a crucial imaging parameter when estimating blood signal enhancement in TOF-MRA. To directly compute blood delivery time from blood velocity, one would need a detailed velocity profile of the blood and its path along the arterial tree together with the exact slab prescription for each scan. While this is not feasible, we can find an upper bound on the blood delivery time expected for pial arteries using estimates of arterial transit time used in arterial spin labelling (ASL) (Detre et al., 1992) . The *arterial transit time*, which includes the transport of blood water spins from the large carotid arteries in the neck through the pial arterial vasculature and the capillaries into the tissue, is estimated to be between 500 ms and

1500 ms in healthy grey matter (Alsop et al., 2015). Since the coverage or slab thickness in TOF-MRA is usually kept small to minimize blood delivery time by shortening the path-length of the vessel contained within the slab (Parker et al., 1991), and because we are focused here on the pial vasculature, we have limited our considerations to a maximum blood delivery time of 1000 ms, with values of few hundreds of milliseconds being more likely.

In summary, targeting pial arteries places us into an imaging regime of mesoscopic vessels (50–300 µm diameter) in a complex branching pattern on a folded surface with blood velocities of 10–50 mm/s and blood delivery times of 200−700 ms. When revisiting the theory behind TOF-MRA for mesoscopic pial arteries, whose diameters are at the size of the imaging voxels or smaller, we thus need to consider partial volume effects, and take into account that: (i) there is no preferential vessel orientation; (ii) while the blood delivery times are long relative to macroscopic arteries, they are still sufficiently short that the blood arrives in the pial arteries in a small fraction of the overall acquisition time; and (iii) the blood passes swiftly through each voxel (i.e. in a time which is short relative to commonly used repetition times).

Flow-related enhancement

Before discussing the effects of vessel size, we briefly revisit the fundamental theory of the flow-related enhancement effect used in TOF-MRA. Taking into account the specific properties of pial arteries, we will then extend the classical description to this new regime. In general, TOF-MRA creates high signal intensities in arteries using inflowing blood as an endogenous contrast agent. The object magnetization—created through the interaction between the quantum mechanical spins of water protons and the magnetic field—provides the signal source (or magnetization) accessed via excitation with radiofrequency (RF) waves (called RF pulses) and the reception of 'echo' signals emitted by the sample around the same frequency. The T_1-contrast in TOF-MRA is based on the difference in the steady-state magnetization of static tissue, which is continuously saturated by RF pulses during the imaging, and the increased or enhanced longitudinal magnetization of inflowing blood water spins, which have experienced no or few RF pulses. In other words, in TOF-MRA we see enhancement for blood that flows into the imaging volume. The steady-state longitudinal magnetization $M_{z\mathrm{S}}^{tissue}$ of static tissue imaged with a (spoiled) FLASH sequence can be calculated (Brown et al., 2014a) using the Ernst equation:

$$M_{z\mathrm{S}}^{\mathrm{tissue}} = \frac{M_0(1-\mathrm{e}^{-T_\mathrm{R}/T_1^{\mathrm{tissue}}})}{1-\mathrm{e}^{-T_\mathrm{R}/T_1^{\mathrm{tissue}}}\cdot\cos\theta}, \qquad \text{Eq. (1)}$$

with M_0 being the thermal equilibrium magnetization before any radiofrequency (RF) pulses, T_R the repetition time, θ the excitation flip angle, and T_1^{tissue} the longitudinal relaxation time of the tissue.

To generate a TOF contrast, a higher flip angle than the optimal Ernst angle (Ernst and Anderson, 1966) is chosen to decrease or suppress the tissue longitudinal magnetization relative to

the thermal equilibrium value. The flowing blood water spins entering into the excited volume are fully relaxed, and as they flow through the imaging volume their longitudinal magnetization M_z^{blood} just before the nth RF pulse is (Brown et al., 2014a):

$$M_z^{\mathrm{blood}}(n_{\mathrm{RF}}) = M_{z\mathrm{S}}^{\mathrm{blood}} + \left(\left(e^{-\frac{T_{\mathrm{R}}}{T_1^{\mathrm{blood}}}}\right) \cdot \cos\theta\right)^{n_{\mathrm{RF}}-1} \cdot \left(M_0 - M_{z\mathrm{S}}^{\mathrm{blood}}\right). \qquad \text{Eq. (2)}$$

The number of RF pulses experienced by the blood, $n_{\mathrm{RF}} = t_{\mathrm{delivery}}/T_{\mathrm{R}}$, depends on the blood delivery time t_{delivery}, i.e. the time it takes the blood spins from entering the imaging volume to reaching the target vessel, and the repetition time T_{R}. Hence, the longitudinal magnetization of the blood water spins is an exponentially decaying function of the number of applied RF pulses, and inversely related to the blood delivery time. We define the flow-related enhancement (FRE), which is the fundamental contrast mechanism in TOF-MRA, as the difference in blood longitudinal magnetization and surrounding tissue signal relative to the tissue signal (Al-Kwifi et al., 2002):

$$FRE(n_{\mathrm{RF}}) = \frac{M_z^{\mathrm{blood}}(n_{\mathrm{RF}}) - M_{z\mathrm{S}}^{\mathrm{tissue}}}{M_{z\mathrm{S}}^{\mathrm{tissue}}}. \qquad \text{Eq. (3)}$$

In classical descriptions of the FRE effect (Brown et al., 2014a; Carr and Carroll, 2012), significant emphasis is placed on the effect of multiple "velocity segments" within a slice in the 2D imaging case. Using the simplified plug-flow model, where the cross-sectional profile of blood velocity within the vessel is constant and effects such as drag along the vessel wall are not considered, these segments can be described as 'disks' of blood that do not completely traverse through the full slice within one T_{R}, and, thus, only a fraction of the blood in the slice is replaced. Consequently, estimation of the FRE effect would then need to accommodate contribution from multiple 'disks' that have experienced 1 to k RF pulses. In the case of 3D imaging as employed here, multiple velocity segments within one voxel are generally not considered, as the voxel sizes in 3D are often smaller than the slice thickness in 2D imaging and it is assumed that the blood completely traverses through a voxel each T_{R}. However, the question arises whether this assumption holds for pial arteries, where blood velocity is considerably lower than in intracranial arteries (Figure 2). To comprehensively answer this question, we have computed the *blood dwell time*[2], i.e. the average time it takes the blood to traverse a voxel, as a function of blood velocity and voxel size (Figure 2). For reference, the blood velocity estimates from the three studies mentioned above (Bouvy et al., 2016; Kobari et al., 1984; Nagaoka and Yoshida, 2006) have been added in this plot as horizontal white lines. For the voxel sizes of interest here, i.e. 50–300 µm, blood dwell times are, for all but the slowest flows, well below commonly used repetition times (Brown et al., 2014a; Carr and Carroll, 2012; Ladd, 2007; von Morze et al., 2007). Thus, in a first

[2] Note that the blood dwell time is inversely related to the critical velocity in 2D MRA but does not need to assume a specific T_{R} value.

approximation using the plug-flow model, it is not necessary to include several velocity segments for the voxel sizes of interest when considering pial arteries, as one might expect from classical treatments, and the FRE effect can be described by equations (Eq. (1) – (Eq. (3), simplifying our characterization of FRE for these vessels. When considering the effect of more complex flow patterns, it is important to bear in mind that the arteries targeted here are only one-voxel thick, and signals are integrated across the whole artery.

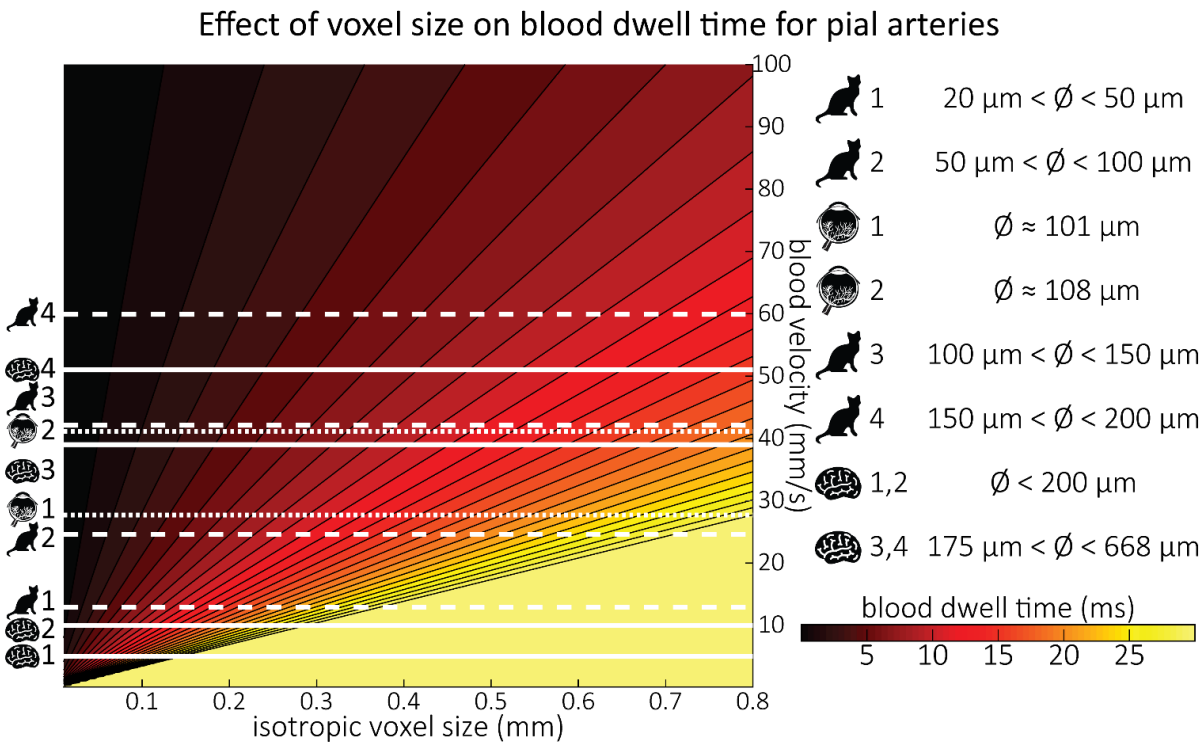

Figure 2: Blood dwell time (ms) as a function of blood velocity and voxel size. For small voxel sizes, blood dwell times are short even for low blood velocities. The horizontal white lines indicate blood velocities reported in humans (solid lines) in the centrum semiovale (1&2) and the basal ganglia (3&4) (Bouvy et al., 2016), in cats (dashed lines) for various pial artery diameters (Kobari et al., 1984), and human retina (dotted lines) (Nagaoka and Yoshida, 2006). For reference, red blood cells in the capillaries are estimated to move at approximately 1 mm/s (Cipolla, 2009; Wei et al., 1993), whereas blood velocities in the major cerebral arteries can reach 1000 mm/s (Lee et al., 1997; Molinari et al., 2006).

Based on these equations, optimal T_{R} and excitation flip angle values (θ) can be calculated for the blood delivery times under consideration (Figure 3). To better illustrate the regime of small arteries, we have illustrated the effect of either flip angle or T_R while keeping the other parameter values fixed to the value that was ultimately used in the experiments; although both parameters can also be optimized simultaneously (Haacke et al., 1990). Supplementary Figure 3 further delineates the interdependency between flip angle and T_R within a parameter range commonly used for TOF imaging at ultra-high field (Kang et al., 2010; Stamm et al., 2013; von Morze et al., 2007). Note how longer T_{R} values still provide an FRE effect even at very long blood delivery times, whereas using shorter T_{R} values can suppress the FRE effect (Figure 3, left). Similarly, at lower flip angles the FRE effect is still

present for long blood delivery times, but it is not available anymore at larger flip angles, which, however, would give maximum FRE for shorter blood delivery times (Figure 3, right). Due to the non-linear relationships of both blood delivery time and flip angle with FRE, the optimal imaging parameters deviate considerably when comparing blood delivery times of 100 ms and 300 ms, but the differences between 300 ms and 1000 ms are less pronounced. In the following simulations and measurements, we have thus used a T_R value of 20 ms, i.e. a value only slightly longer than the readout of the high-resolution TOF acquisitions, which allowed time-efficient data acquisition, and a nominal excitation flip angle of 18°. From a practical standpoint, these values are also favorable as the low flip angle reduces the specific absorption rate (Fiedler et al., 2018) and the long T_R value decreases the potential for peripheral nerve stimulation (Mansfield and Harvey, 1993).

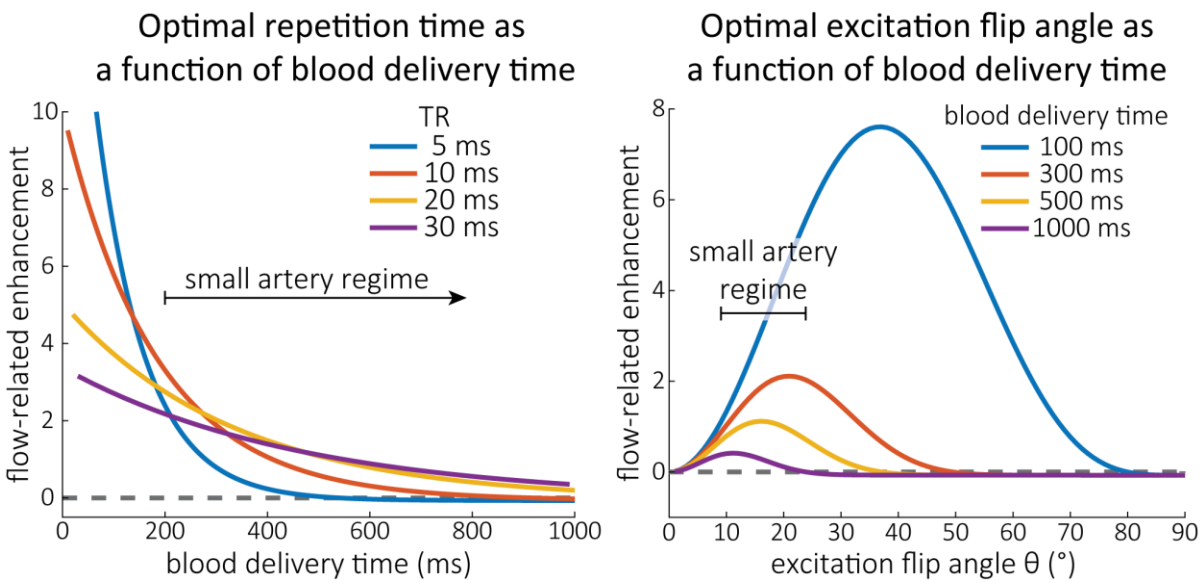

Figure 3: Optimal imaging parameters for small arteries. LEFT: Flow-related enhancement (FRE) was simulated as a function of blood delivery time for different repetition times assuming an excitation flip angle of 18° and longitudinal relaxation times of blood and tissue of 2100 ms and 1950 ms at 7 T, respectively. Overall, FRE decreases with increasing blood delivery times. In the small vessel regime, i.e. at blood delivery times > 200 ms, longer repetition times result in higher FRE than shorter repetition times. RIGHT: FRE was simulated as a function of excitation flip angle for different blood delivery times assuming a T_R value of 20 ms and longitudinal relaxation rates as above. The excitation flip angle that maximizes FRE for longer blood delivery times is lower than the excitation flip angle that maximizes FRE for shorter blood delivery times, and often the optimal excitation flip angle is close to the Ernst angle for longer blood delivery times (Ernst angle: 8.2°; optimal excitation flip angles: 37° (100 ms), 21° (300 ms), 16° (500 ms), 11° (1000 ms)).

The optimizations presented so far have assumed that the voxel is fully filled with blood. However, in the case of pial arteries, vessel diameters are often comparable to or smaller than the voxel size. In the next section, we will therefore investigate the individual contributions of blood delivery times and voxel size to the overall FRE in pial arteries. We will introduce a model that consider the partial volume effects of blood and tissue to allow us to decide whether imaging of pial arteries is

limited by the physiological properties of the brain vasculature, i.e. blood flow rates, or the available image resolution.

Introducing a partial-volume model

To account for the effect of voxel volume on the FRE, the total longitudinal magnetization M_z needs to also consider the number of spins contained within in a voxel (Du et al., 1996; Venkatesan and Haacke, 1997). A simple approximation can be obtained by scaling the longitudinal magnetization with the voxel volume (Venkatesan and Haacke, 1997)[3]. To then include partial volume effects, the total longitudinal magnetization in a voxel M_z^{total} becomes the sum of the contributions from the stationary tissue $M_{z\text{S}}^{\text{tissue}}$ and the inflowing blood M_z^{blood}, weighted by their respective volume fractions V_{rel}:

$$M_z^{\text{total}} = V_{\text{rel}}^{\text{blood}} \cdot M_z^{\text{blood}} + V_{\text{rel}}^{\text{tissue}} \cdot M_{z\text{S}}^{\text{tissue}}. \qquad \text{Eq. (4)}$$

For simplicity, we assume a single vessel is located at the center of the voxel and approximate it to be a cylinder with diameter d_{vessel} and length l_{voxel} of an assumed isotropic voxel along one side. The relative volume fraction of blood $V_{\text{rel}}^{\text{blood}}$ is the ratio of vessel volume within the voxel to total voxel volume (see section *Estimation of vessel-volume fraction* in the Supplementary Material), and the tissue volume fraction $V_{\text{rel}}^{\text{tissue}}$ is the remainder that is not filled with blood, or

$$V_{\text{rel}}^{\text{tissue}} = 1 - V_{\text{rel}}^{\text{blood}}. \qquad \text{Eq. (5)}$$

We can now replace the blood magnetization in equation Eq. (3) with the total longitudinal magnetization of the voxel to compute the FRE as a function of vessel-volume fraction:

$$\text{FRE}_{\text{PV}}(n_{\text{RF}}, l_{\text{voxel}}, d_{\text{vessel}}) = \frac{M_z^{\text{total}}(n_{\text{RF}}, l_{\text{voxel}}, d_{\text{vessel}}) - M_{z\text{S}}^{\text{tissue}}}{M_{z\text{S}}^{\text{tissue}}}. \qquad \text{Eq. (6)}^{4}$$

Figure 4 illustrates the partial-volume FRE (FRE_{PV}) assuming a pial artery diameter (d_{vessel}) of 200 µm, a T_{R} value of 20 ms, an excitation flip angle of 18 °, and longitudinal relaxation times of blood and tissue of 2100 ms and 1950 ms, respectively (Huber, 2014, Table 2.1). Therein, two prominent regimes appear along the voxel size axis: (i) the blood-delivery-time dominated regime, where as long as the voxel is completely filled with blood, i.e. $l_{\text{voxel}} < \cos\frac{\pi}{4} \cdot d_{\text{vessel}}$, the voxel size has no impact on the FRE, and the FRE is solely an exponential function of the blood delivery time (Eq. (2), Figure 3); (ii) the voxel-size dominated regime, where if the vessel is smaller than the voxel, the FRE also depends quadratically on the voxel size (see *Estimation of vessel-volume fraction*). Note that our partial-volume model encompasses both regimes, and because the $\text{FRE}_{2\text{C}}$ definition reverts to the classical FRE definition for larger-than-voxel-sized vessels, we will from now on use FRE synonymously with $\text{FRE}_{2\text{C}}$. In theory, a reduction in blood delivery time increases the FRE in both

[3] Note that this does not affect the relative FRE definition presented in Eq. (3), as the effect of total voxel volume cancels out.

[4] Note that this can also be written as $\text{FRE}_{2\text{C}}(n_{\text{RF}}, l_{\text{voxel}}, d_{\text{vessel}}) = V_{\text{rel}}^{\text{blood}}(l_{\text{voxel}}, d_{\text{vessel}}) \cdot \text{FRE}(n_{\text{RF}})$.

regimes, and—if the vessel is smaller than the voxel—so would a reduction in voxel size. In practice, a reduction in slab thickness—which is the default strategy in classical TOF-MRA to reduce blood delivery time— might not provide substantial FRE increases for pial arteries. This is due to their convoluted geometry (see section *Anatomical architecture of the pial arterial vasculature*), where a reduction in slab thickness may not necessarily reduce the vessel segment length if the majority of the artery is still contained within the smaller slab. Thus, given the small arterial diameter, reducing the voxel size is a much more promising avenue when imaging the pial arterial vasculature.

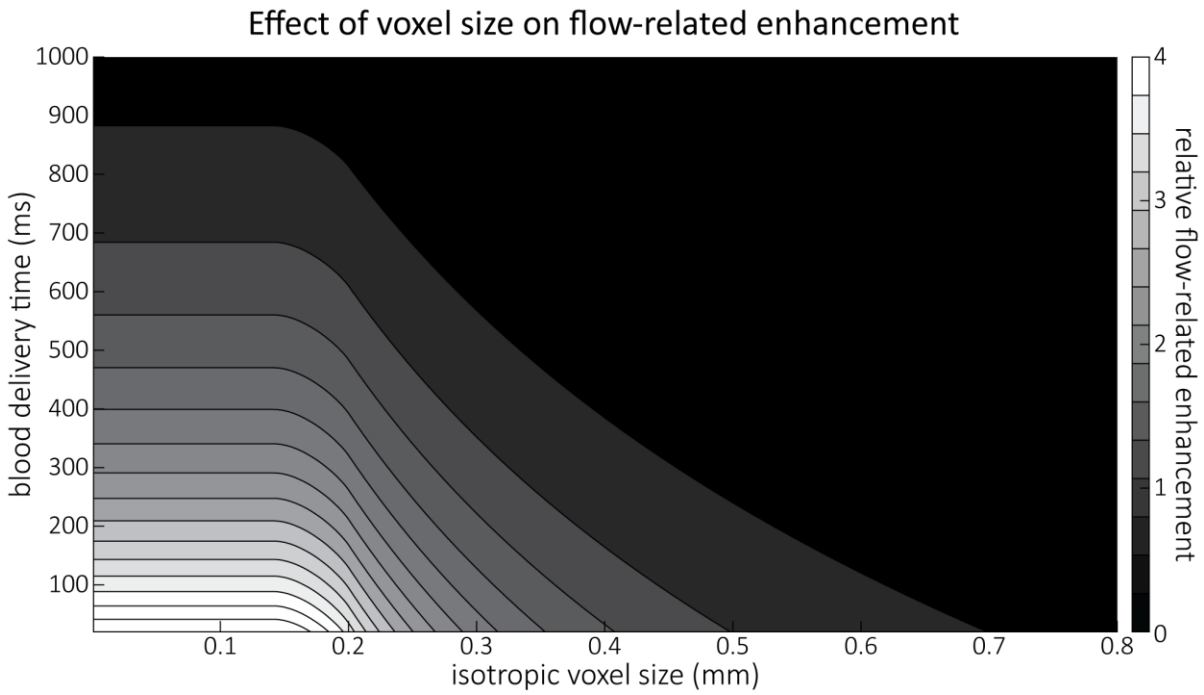

Figure 4: Effect of voxel size and blood delivery time on the relative flow-related enhancement (FRE), assuming a pial artery diameter of 200 µm. The relative FRE represents the signal intensity in the voxel containing the artery relative to the surrounding tissue (Eq. (3)). For example, an FRE of 0 would indicate equal intensity, and an FRE of 1 would indicate twice the signal level in the voxel compared to the surrounding tissue. The FRE decreases with blood delivery time due to more signal attenuation (Eq. (2)) and with voxel size due to more partial volume effects (Eq. (4)).

Inflow-artefacts in sinuses and pial veins

Inflow in large pial veins and the sagittal and transverse sinuses can cause flow-related enhancement in these non-arterial vessels. One common strategy to remove this unwanted signal enhancement is to apply venous suppression pulses during the data acquisition, which saturate bloods spins outside the imaging slab. Disadvantages of this technique are the technical challenges of applying these pulses at ultra-high field due to constraints of the specific absorption rate (SAR) and the necessary increase in acquisition time (Conolly et al., 1988; Heverhagen et al., 2008; Johst et al., 2012; Maderwald et al., 2008; Schmitter et al., 2012; Zhang et al., 2015). In addition, optimal positioning of the saturation slab in the case of pial arteries requires further investigation, and in particular supressing signal from the superior sagittal sinus without interfering in the imaging of the pial arteries vasculature at the top of

the cortex might prove challenging. Furthermore, this venous saturation strategy is based on the assumption that arterial blood is traveling head-wards while venous blood is drained foot-wards. For the complex and convoluted trajectory of pial vessels this directionality-based saturation might be oversimplified, particularly when considering the higher-order branches of the pial arteries and veins on the cortical surface.

Inspired by techniques to simultaneously acquire a TOF image for angiography and a susceptibility-weighted image for venography (Bae et al., 2010; Deistung et al., 2009; Du et al., 1994; Du and Jin, 2008), we set out to explore the possibility of removing unwanted venous structures from the segmentation of the pial arterial vasculature during data postprocessing. Because arteries filled with oxygenated blood have T_2^*-values similar to tissue, while veins have much shorter T_2^*-values due to the presence of deoxygenated blood (Pauling and Coryell, 1936; Peters et al., 2007; Uludağ et al., 2009; Zhao et al., 2007), we used this criterion to remove vessels with short T_2^* values from the segmentation (see *Data Analysis* for details). In addition, we also explored whether unwanted venous structures in the high-resolution TOF images—where a two-echo acquisition is not feasible due to the longer readout—can be removed based on detecting them in a lower-resolution image.

Velocity- and TE-dependent vessel displacement artifacts

While isotropic 3D TOF-MRA provides detailed information on the vessel position, the continuous motion of blood during image acquisition can lead to vessel displacement artefacts in the phase-encoding directions (Brown et al., 2014b; Parker et al., 2003). The magnitude of this misregistration artefact depends on the time elapsed between the time of the phase-encoding blip (t_{pe}) and the echo time (T_{E}) and on the blood velocity in the primary phase-encoding direction y, v_y:

$$\Delta y_{\mathrm{displ}} = -v_y \cdot \left(T_{\mathrm{E}} - t_{\mathrm{pe}}\right). \qquad \text{Eq. (7)}$$

A similar relationship for $\Delta z_{\mathrm{displ}}$ exists for the secondary phase-encoding direction z. According to this relationship, and based on the reported velocity range in Figure 2, vessel displacements in the phase-encoding directions between 25 µm and 250 µm for a time delay $\left(T_{\mathrm{E}} - t_{\mathrm{pe}}\right)$ of 5 ms can be expected. Flow-compensation gradients can correct for the effect of constant velocities (Parker et al., 2003), but the required large gradient lobes for high-resolution applications would substantially increase the T_{E}, and, consequently, reduce the SNR. For these reasons, no flow compensation in the phase-encoding-directions was used for the high-resolution images in this study. However, we do assess the extent of vessel displacement using a two-echo low-resolution acquisition.

Considerations for imaging the pial arterial vasculature

We have identified voxel size as the key parameter for imaging pial arteries. While the benefit of smaller voxels was conceptually known and empirically shown before (Haacke et al., 1990; Mattern et

al., 2018; von Morze et al., 2007), clear guidelines on how small is sufficiently small and how strongly the FRE increases with decreasing voxel size were not established. We can now conclude that the voxel size should be at least the size of the pial artery, i.e. somewhere between 50 µm and 280 µm in our case, and ideally around 70 % of that, i.e. 35 µm to 200 µm. While this is challenging in practice, the strong increase in FRE especially when voxel sizes are similar to vessel size makes a reduction of even only 10 or 20 µm worthwhile for imaging pial arteries. Further, we have seen that slow blood velocities are an unlikely explanation for loss of FRE in small vessels, because (i) blood delivery times to pial arteries are sufficiently short due to the perhaps surprisingly fast blood flow in these mesoscopic vessels, (ii) the effect of blood delivery time on FRE decreases with increasing blood delivery times, and (iii) the addition of partial volume effects to the FRE estimation predicts the often observed drastic loss of contrast in small vessels. Thus, we expect a reduction in voxel size to directly translate into an increased sensitivity for small pial arteries.

Results

Effect of voxel size on flow-related enhancement

To investigate the effect of voxel size on vessel FRE, we acquired data at four different voxel sizes ranging from 0.8 mm to 0.3 mm isotropic resolution, adjusting only the encoding matrix, with imaging parameters being otherwise identical (FOV, TR, TE, flip angle, R, slab thickness, see section *Data acquisition*). The total acquisition time increases from less than 2 minutes for the lowest resolution scan to over 6 minutes for the highest resolution scan as a result. Figure 5 shows thin maximum intensity projections of a small artery. While the artery is not detectable at the largest voxel size, it slowly emerges as the voxel size decreases and approaches the vessel size. Presumably, this is driven by the considerable increase in FRE as seen in the single slice view (Figure 5, small inserts). Accordingly, the FRE computed from the vessel mask for the smallest part of the vessel (Figure 5, red mask) increases substantially with decreasing voxel size. More precisely, reducing the voxel size from 0.8 mm, 0.5 mm or 0.4 mm to 0.3 mm increases the FRE by 2900 %, 165 % and 85 %, respectively. Assuming an arterial diameter of 300 µm partial-volume FRE model (*Introducing a partial-volume model*) would predict similar ratios of 611%, 178% and 78%.

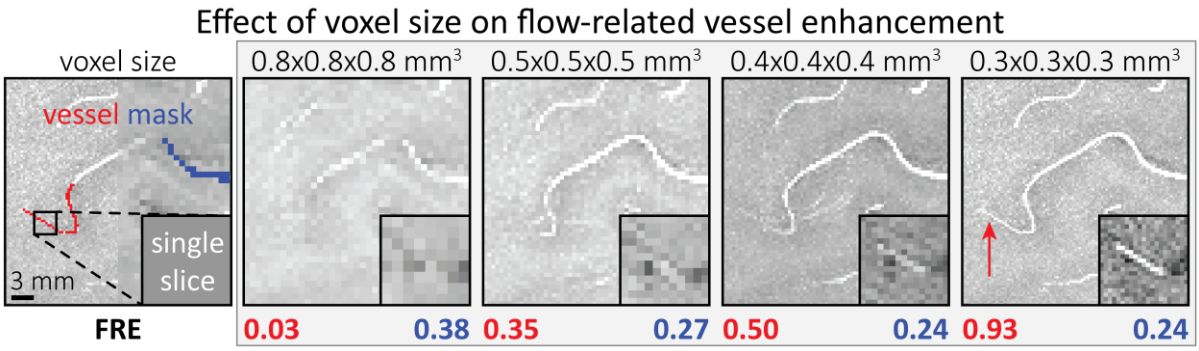

Figure 5: Effect of voxel size on flow-related vessel enhancement. Thin axial maximum intensity projections containing a small artery acquired with different voxel sizes ranging from 0.8 mm to 0.3 mm isotropic are shown. The FRE is estimated using the mean intensity value within the vessel masks depicted on the left, and the mean intensity values of the surrounding tissue. The small insert shows a section of the artery as it lies within a single slice. A reduction in voxel size is accompanied by a corresponding increase in FRE (red mask), whereas no further increase is obtained once the voxel size is equal or smaller than the vessel size (blue mask).

However, as long as the vessel is larger than the voxel (Figure 5, blue mask), the relative FRE does not change with resolution (see also *Effect of FRE Definition and Interaction with Partial-Volume Model* in the Supplementary Material). To illustrate the gain in sensitivity to detect smaller arteries, we have estimated the relative increase of the total length of the segmented vasculature (Supplementary Figure 9): reducing the voxel size from 0.8 mm to 0.5 mm isotropic increases the skeleton length by 44 %, reducing the voxel size from 0.5 mm to 0.4 mm isotropic increases the skeleton length by 28 %, and reducing the voxel size from 0.4 mm to 0.3 mm isotropic increases the skeleton length by 31 % In

summary, when imaging small pial arteries, these data support the hypothesis that it is primarily the voxel size, not blood delivery time, which determines whether vessels can be resolved.

Imaging the pial arterial vasculature

Based on these results, we then proceeded to image the pial arterial vasculature at a much higher resolution of 0.16 mm isotropic, to verify that small pial arteries can be visualised using a TOF-based contrast. Figure 6 shows the axial maximum intensity projection overlaid with a vessel segmentation on the left, a coronal projection of the central part of the brain, a sagittal projection and a 3D view of the segmentation on the right. Note the numerous right-angled branches emerging from the parent artery, indicating the increased sensitivity to small pial arteries, and the overall high vessel density compared with acquisitions performed at conventional resolutions (Bernier et al., 2018; Brown et al., 2014a; Chen et al., 2018; Ladd, 2007; Mattern et al., 2018; Schulz et al., 2016; Stucht et al., 2015; von Morze et al., 2007; Wright et al., 2013).

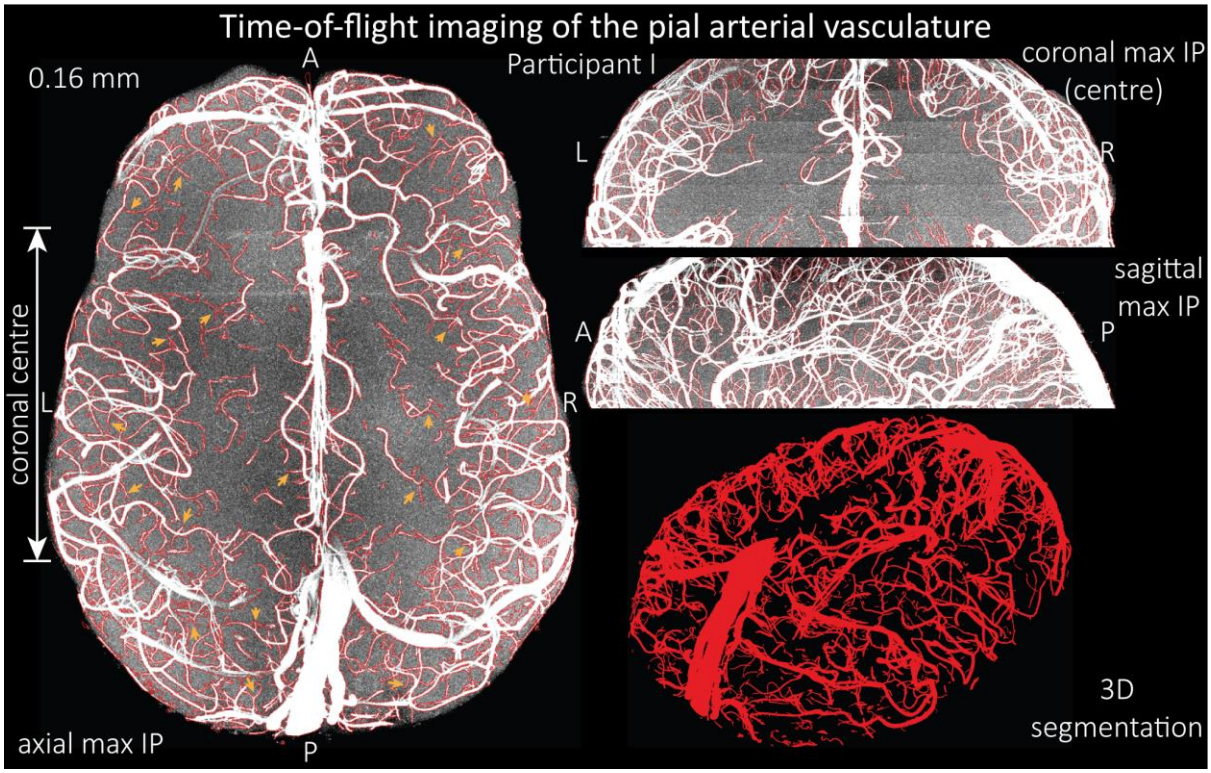

Figure 6: Time-of-flight imaging of the pial arterial vasculature at 0.16 mm isotropic resolution and 50 mm coverage in the head-foot direction. LEFT: Axial maximum intensity projection and outline of the vessel segmentation overlaid in red. Examples of the numerous right-angled branches are indicated by orange arrows. RIGHT: Coronal maximum intensity projection and segmentation of the central part of the brain (top), sagittal maximum intensity projection and segmentation (middle), and 3D view of the vessel segmentation (bottom).

The horizontal lines in the background presumably stem from stacking multiple slabs containing slightly different imaging volumes and potentially imperfect slab profiles. Data acquired with the same parameters in an additional participant is shown in Supplementary Figure 4. For reference, data from

both participants without the overlay of the segmentation are presented in Supplementary Figure 5 and 6.

To assess the benefit of even higher resolution, we acquired time-of-flight data with an isotropic voxel size of 140 µm in a second participant using prospective motion correction (Mattern et al., 2018)Figure 7 to reduce motion artefacts given the even longer acquisition time and higher resolution (Figure 7).

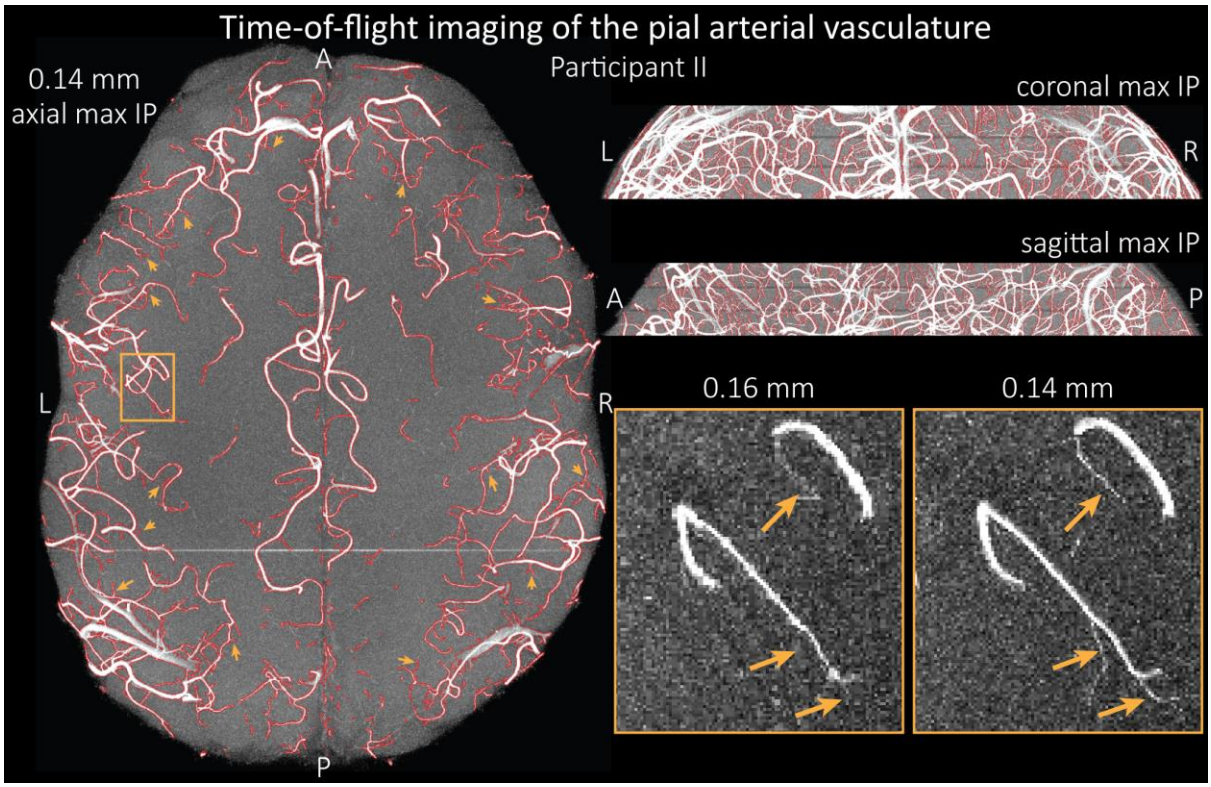

Figure 7: Time-of-flight imaging of the pial arterial vasculature at 0.14 mm isotropic resolution and 19.6 mm coverage in the foot-head direction. LEFT: Axial maximum intensity projection and outline of the vessel segmentation overlaid in red. Examples of the numerous right-angled branches are indicated by orange arrows. RIGHT: Coronal maximum intensity projection and segmentation (top) and sagittal maximum intensity projection and segmentation (middle). A comparison of 0.16 mm and 0.14 mm voxel size (bottom) shows several vessels visible only at the higher resolution. The location of the insert is indicated on the axial maximum intensity projection on the left. Note that for this comparison the coverage of the 0.14 mm data was matched to the smaller coverage of the 0.16 mm data.

The axial maximum intensity projection illustrates the large number of right-angled branches visible at this resolution. Similarly, the coronal and sagittal projections demonstrate the high density of the vasculature at this level. Note that unwanted signal in non-arterial vessels such as pial veins and the superior sagittal sinus has been removed using an auxiliary acquisition as described in the section *Removal of pial veins* below. We have also acquired one single slab with an isotropic voxel size of 0.16 mm with prospective motion correction for this participant in the same session to compare to the acquisition with 0.14 mm isotropic voxel size and to test whether any gains in FRE are still possible at this level of the vascular tree. Indeed, the reduction in voxel volume by 33 % revealed additional

small branches connected to larger arteries (see also Supplementary Figure 8). For this example, we found an overall increase in skeleton length of 14 % (see also Supplementary Figure 9). In summary, we have found that reducing voxel sizes increases FRE up to at least 0.14 mm isotropic resolution and conclude that partial volume effects are the main contributor to FRE loss in small arteries.

Vessel displacement artefacts

The vessel displacement artefacts in the phase-encoding directions due to blood motion are illustrated in Figure 8 using a two-echo TOF acquisition from a fourth participant. At a delay time of 10 ms between phase encoding and echo time, the observed displacement of approximately 2 mm in some of the larger arteries would correspond to a blood velocity of 200 mm/s, which is well within the expected range (Figure 2). For the smallest arteries, a displacement of one voxel (0.4 mm) can be observed, indicative of blood velocities of 40 mm/s. Note that the vessel displacement can be observed in all arteries visible at this resolution, indicating high blood velocities throughout much of the pial arterial vasculature. Thus, assuming a blood velocity of 40 mm/s (Figure 2) and a delay time of 5 ms for the high-resolution acquisitions (Figure 6), vessel displacements of 0.2 mm are possible, representing a shift of 1–2 voxels.

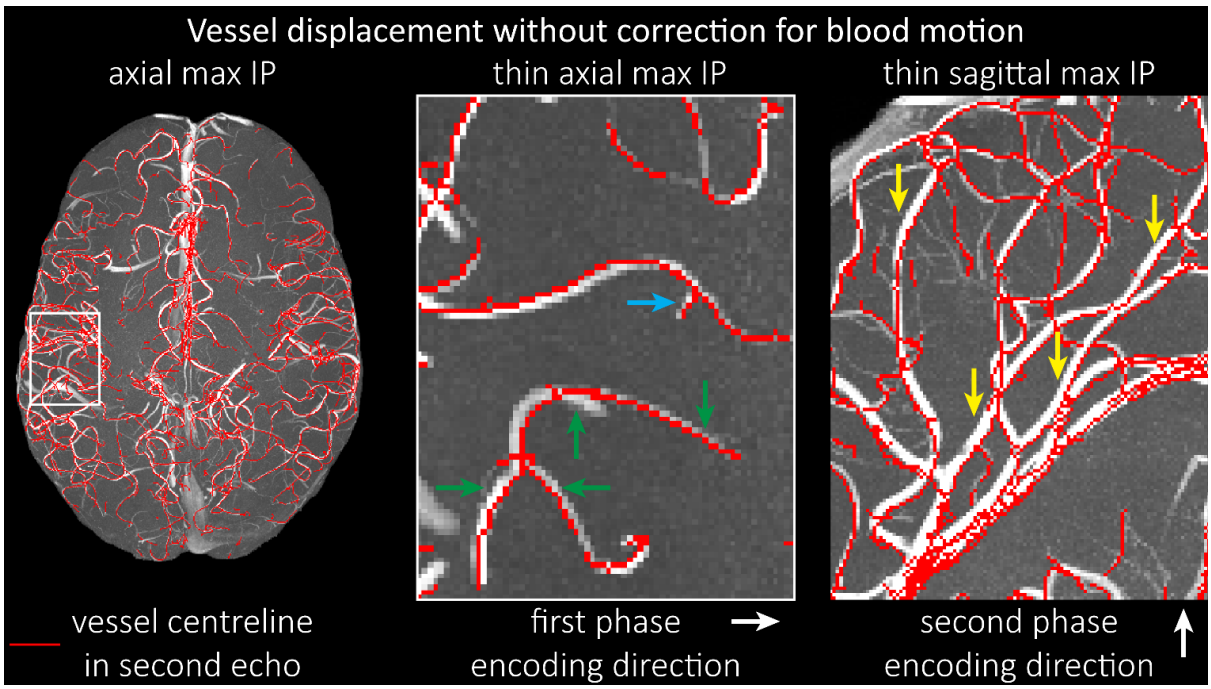

Figure 8: Vessel displacement without correction for blood motion. The vessel displacement is illustrated using a maximum intensity projection of the first, flow compensated echo of a two-echo TOF acquisition with the vessel centreline of the second echo without flow-compensation overlaid in red. Strong displacements in both phase-encoding directions are present resulting in complex vessel shift patterns (green arrows). While furthest vessel displacements are observed in large arteries with faster flow (yellow arrows), considerable displacements arise even in smaller arteries (blue arrow).

Removal of pial veins

Inflow in large pial veins and the superior sagittal and transverse sinuses can cause a flow-related enhancement in these non-arterial vessels (Figure 9, left). The higher concentration of deoxygenated haemoglobin in these vessels leads to shorter T_2^* values (Pauling and Coryell, 1936), which can be estimated using a two-echo TOF acquisition (see also *Inflow-artefacts in sinuses and pial veins*). These vessels can be identified in the segmentation based on their T_2^* values (Figure 9, left), and removed from the angiogram (Figure 9, right) (Bae et al., 2010; Deistung et al., 2009; Du et al., 1994; Du and Jin, 2008). Predominantly, large vessels which exhibited an inhomogeneous intensity profile and a steep loss of intensity at the slab boundary were identified as non-arterial (Figure 9, left). Further, we also explored the option of removing unwanted venous vessels from the high-resolution TOF image (Figure 7) using a low-resolution two-echo TOF (not shown). This indeed allowed us to remove the strong signal enhancement in the sagittal sinuses and numerous larger veins, although some small veins, which are characterised by inhomogeneous intensity profiles and can be detected visually by experienced raters, remain.

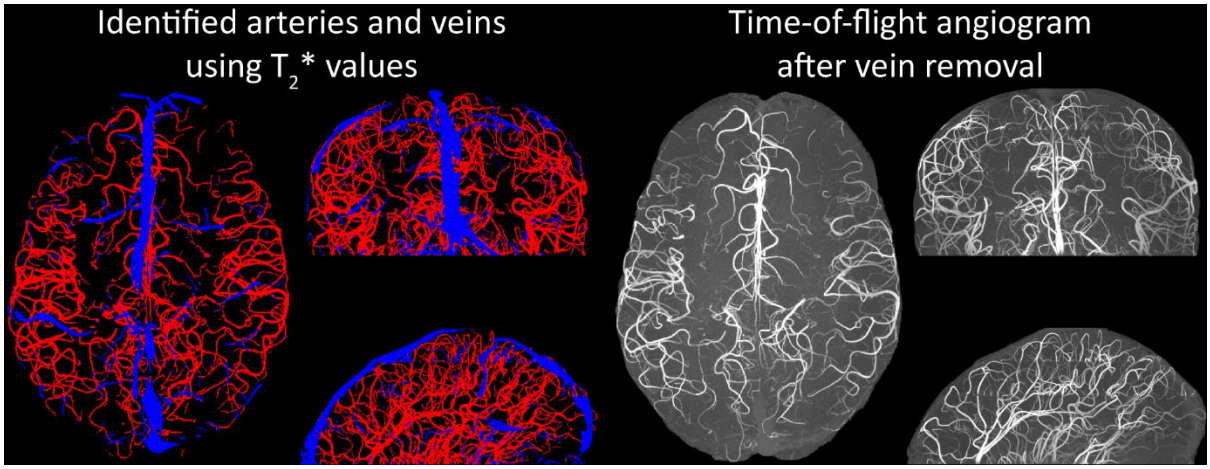

Figure 9: Removal of non-arterial vessels in time-of-flight imaging. LEFT: Segmentation of arteries (red) and veins (blue) using T_2^* estimates. RIGHT: Time-of-flight angiogram after vein removal.

Discussion

A new perspective on imaging the pial arterial vasculature

We have outlined the theoretical components and provided empirical evidence for geometrically accurate imaging of the pial arterial vasculature of the human brain *in vivo*. We found that reducing the voxel size increases the vessel contrast when imaging the pial arterial vasculature of the human brain, in contrast to previous theoretical and empirical treatments of the effect of voxel size on vessel contrast (Du et al., 1993, 1996; Venkatesan and Haacke, 1997). Further, we could not confirm the common assumption that slow blood flow is the main limiting factor for high-resolution time-of-flight imaging (Chen et al., 2018; Haacke et al., 1990; Masaryk et al., 1989; Mut et al., 2014; Park et al., 2020; Parker et al., 1991; Wilms et al., 2001; Wright et al., 2013), but instead found adequate signal levels even in smallest pial arteries given sufficiently small voxels (Figure 7). Both effects are driven by non-linear relationships which might have contributed to their over- and underestimation in the literature. In short, flow-related enhancement (FRE) depends exponentially on blood delivery times (Figure 3), such that it *decreases* for longer blood delivery times, and quadratically on voxel size (Figure 4), such that it *increases* for smaller voxels—i.e. the imaging regime of pial arteries.

Extending classical FRE treatments to the pial vasculature

There are several major modifications in our approach to this topic that might explain why, in contrast to predictions from classical FRE treatments, it is indeed possible to image pial arteries. For instance, the definition of vessel contrast or flow-related enhancement is often stated as an absolute difference between blood and tissue signal (Brown et al., 2014a; Carr and Carroll, 2012; Du et al., 1993, 1996; Haacke et al., 1990; Venkatesan and Haacke, 1997). Here, however, we follow the approach of Al-Kwifi et al. (2002) and consider *relative* contrast. While this distinction may seem to be semantic, the effect of voxel volume on FRE for these two definitions is exactly opposite: Du et al. (1996) concluded that larger voxel size increases the (absolute) vessel-background contrast, whereas here we predict an increase in relative FRE for small arteries with decreasing voxel size. Therefore, predictions of the depiction of small arteries with decreasing voxel size differ depending on whether one is considering absolute contrast, i.e. difference in longitudinal magnetization, or relative contrast, i.e. contrast differences independent of total voxel size. Importantly, this prediction changes for large arteries where the voxel contains only vessel lumen, in which case the relative FRE remains constant across voxel sizes, but the absolute FRE increases with voxel size (Supplementary Figure 2). Overall, the interpretations of relative and absolute FRE differ, and one measure may be more appropriate for certain applications than the other. Absolute FRE describes the difference in magnetization and is thus tightly linked to the underlying physical mechanism. Relative FRE, however, describes the image contrast and segmentability. If blood and tissue magnetization are equal, both contrast measures

would equal zero and indicate that no contrast difference is present. However, when there is signal in the vessel and as the tissue magnetization approaches zero, the absolute FRE approaches the blood magnetization (assuming no partial-volume effects), whereas the relative FRE approaches infinity. While this infinite relative FRE does not directly relate to the underlying physical process of 'infinite' signal enhancement through inflowing blood, it instead characterizes the segmentability of the image in that an image with zero intensity in the background and non-zero values in the structures of interest can be segmented perfectly and trivially. Accordingly, numerous empirical observations (Al-Kwifi et al., 2002; Bouvy et al., 2014; Haacke et al., 1990; Ladd, 2007; Mattern et al., 2018; von Morze et al., 2007) including the data provided here (Figure 5, 6 and 7) have shown the benefit of smaller voxel sizes if the aim is to visualize and segment small arteries.

In addition, we also formulated the problem in 3D space taking into account the spatial characteristics of blood vessels in particular, which are in principle elongated, and approximately 1-dimensional structures. Because Venkatesan and Haacke (1997) assumed a 1D image consisting of a row of samples, they predicted *no* impact of voxel size on absolute FRE, despite using the same theory as Du et al. (1996), who operated in 2D space and predicted increased FRE for larger voxel sizes. The image intensity of a voxel with an elongated vessel in its center will scale differently with increasing isotropic voxel size than a voxel containing point-like (0-dimensional) or extended sheet-like (2-dimensional) objects. Note that classical considerations of partial volume effects (Shattuck et al., 2001) cannot be readily applied to vessels, as these treatments usually assume two-dimensional borders of larger structures meeting in a voxel (such as the boundary between two tissue volumes). Thus, not only the FRE definition in terms of absolute or relative contrast, but also the dimensionality and geometry of the assumed tissue content matters. In summary, we have presented a comprehensive theoretical framework for imaging small pial arteries which considers contrast and dimensionality, and from which we can conclude that small voxel sizes are the key ingredient for imaging the pial arterial vasculature.

Imaging limitations

To maximize the sensitivity and accuracy of imaging small pial arteries, challenges regarding vessel localization and imaging noise remain to be investigated. First, the effect of vessel location within the voxel on the FRE needs to be addressed in more detail. Note that in our theoretical treatment we have always assumed a vessel located centrally in the voxel. If a vessel is not centered and instead was split over several voxels, such that its cross-section intersected the voxel border, we would, due to the reduction in relative blood volume fraction (Eq. (4)), expect a reduction in FRE in each containing voxel. However, given that in Fourier imaging used in MRI the voxel grid is arbitrarily placed, previous work (Du et al., 1994; Zhu et al., 2013) has argued that zero-filling could resolve this issue, and would

essentially “re-center” the vessel within a voxel. However, it remains unclear what the optimal zero-filling factor would be. Classical Fourier theory predicts sensitivity gains only up to a zero-filling factor of 2; beyond that, zero-filling is equivalent to interpolation and correlation between samples is introduced (Bartholdi and Ernst, 1973). Nevertheless, slight qualitative improvements in image appearance have been reported for higher zero-filling factors (Du et al., 1994), presumably owing to a smoother representation of the vessels (Bartholdi and Ernst, 1973). In contrast, Mattern et al. (2018) reported no improvement in vessel contrast for their high-resolution data. Ultimately, for each application, e.g. visual evaluation vs. automatic segmentation, the optimal zero-filling factor needs to be determined, balancing image appearance (Du et al., 1994; Zhu et al., 2013) with loss in statistical independence of the image noise across voxels. For example, in Figure 5, when comparing across different voxel sizes, the visual impression might improve with zero-filling. However, it remains unclear whether the same zero-filling factor should be applied for each voxel size, which means that the overall difference in resolution remains, namely a nearly 20-fold reduction in voxel volume when moving from 0.8-mm isotropic to 0.3 mm isotropic voxel size. Alternatively, the same ’zero-filled’ voxel sizes could be used for evaluation, although then nearly 94 % of the samples used to reconstruct the image with 0.8-mm voxel size would be zero-valued for a 0.3-mm isotropic resolution. Consequently, all data presented in this study were reconstructed without zero-filling.

A further challenge for obtaining accurate vessel localization is the vessel displacement (Figure 8) in both phase encoding directions due to blood motion (Figure 4), which restricts the ability to register these images of the arterial vasculature with data from other image modalities. While modifications to the pulse sequence can address this problem (Parker et al., 2003), their practical implementation (e.g. peripheral nerve stimulation (Mansfield and Harvey, 1993)) is limited in the case of small pial arteries (e.g. limits imposed by maximum gradient slew rates or peripheral nerve stimulation (Mansfield and Harvey, 1993)), because the high-resolution acquisitions would require strong flow compensation gradients to be played out in a very short amount of time to ensure sufficiently short echo times needed to retain SNR. Classical approaches to correct apparent tissue displacement stemming from B_0-inhomogeneities such as reversal of the phase-encoding directions (Andersson et al., 2003) cannot be applied here, as the vessel displacement reflects true object motion (Supplementary Figure 10). Note that correction techniques exist to remove displaced vessels from the image (Gulban et al., 2021), but they cannot revert the vessels to their original location. Alternatively, this artefact could also potentially be utilised as a rough measure of blood velocity. Other encoding strategies, such as radial and spiral acquisitions, experience no vessel displacement artefact because phase and frequency encoding take place in the same instant; although a slight blur might be observed instead (Nishimura et al., 1995, 1991). However, both trajectories pose engineering

challenges and much higher demands on hardware and reconstruction algorithms than the Cartesian readouts employed here (Kasper et al., 2018; Shu et al., 2016); particularly to achieve 3D acquisitions with 160 µm isotropic resolution. Provided that the imaging echo times are kept short, the overall size of this effect is small for pial arteries and estimated to be less than two voxel lengths for the imaging protocols used in this study. However, the displacement of feeding arteries with faster velocities can reach values of 1 mm or more (Figure 7), introducing a nonlinear distortion of the arteries depending on the blood velocity and direction. This may be inconsequential for many applications such as those investigating topological features, but may prove challenging when, for example, the aim is to accurately combine the segmentation of the pial vasculature with a segmentation of the cerebral cortical surface.

From a practical perspective when performing the imaging experiments, the required long acquisition times and small voxels make these high-resolution acquisitions particularly vulnerable to image artifacts from subject motion. This has been addressed utilizing a prospective motion correction system (Mattern et al., 2018) to enable the acquisition of TOF data with 0.14 mm isotropic voxel size and over 20 minutes acquisition time per imaging slab. This allowed for the successful correction of head motion of approximately 1 mm over the 60-minute scan session, showing the potential of prospective motion correction at these very high resolutions. Note that for the comparison in Figure 7, one slab with 0.16 mm voxel size was acquired in the same session also using the prospective motion correction system. However, for the data shown in Figure 6 and Supplementary Figure 4, no prospective motion correction was used, and we instead relied on the experienced participants who contributed to this study. We found that the acquisition of TOF data with 0.16 mm isotropic voxel size in under 12 minutes acquisition time per slab possible without discernible motion artifacts, although even with this nearly ideal subject behaviour approximately 1 in 4 scans still had to be discarded and repeated. Motion correction will generally be necessary to acquire data at higher resolution than that presented here. Alternatively, imaging acceleration techniques could be applied (Candes et al., 2006; Griswold et al., 2002; Pruessmann et al., 1999), but because these techniques undersample the imaging data, they come at the cost of lower image SNR and significant reductions in scan times might not be possible. Acquiring these data at even higher field strengths would boost SNR (Edelstein et al., 1986; Pohmann et al., 2016) to partially compensate for SNR losses due to acceleration and may enable faster imaging and/or smaller voxel sizes. This could facilitate the identification of the ultimate limit of the flow-related enhancement effect and identify at which stage of the vascular tree does the blood delivery time become the limiting factor. While Figure 7 indicates the potential for voxel sizes below 0.16 mm, the singular nature of this comparison warrants further investigations.

In general, we have not considered SNR, but only FRE, i.e. the (relative) image contrast, assuming that segmentation algorithms would benefit from higher contrast for smaller arteries. Importantly, the acquisition parameters available to maximize FRE are limited, namely repetition time, flip angle and voxel size. SNR, however, can be improved via numerous avenues independent of these parameters (Brown et al., 2014c; Du et al., 1996; Heverhagen et al., 2008; Parker et al., 1991; Triantafyllou et al., 2011; Venkatesan and Haacke, 1997), the simplest being longer acquisition times. If the aim is to optimize a segmentation outcome for a given acquisition time, the trade-off between contrast and SNR for the specific segmentation algorithm needs to be determined (Klepaczko et al., 2016; Lesage et al., 2009; Moccia et al., 2018; Phellan and Forkert, 2017). Our own—albeit limited—experience has shown that segmentation algorithms (including manual segmentation) can accommodate a perhaps surprising amount of noise using prior knowledge and neighborhood information, making these high-resolution acquisitions possible. Importantly, note that our treatment of the FRE does not suggest that an arbitrarily small voxel size is needed, but instead that voxel sizes appropriate for the arterial diameter of interest are beneficial (in line with the classic "matched-filter" rationale (North, 1963)). Voxels smaller than the arterial diameter would not yield substantial benefits (Figure 5) and may result in SNR reductions that would hinder segmentation performance. Nevertheless, if SNR were also to be considered in the regime of pial arteries, the noise "magnitude bias" due to the effects of multi-channel magnitude-valued data on the noise distribution (Constantinides et al., 1997; Triantafyllou et al., 2011) needs to be accounted for. In particular the low SNR expected in the tissue signal, which in TOF-MRA should ideally be near the noise floor especially for high resolution acquisitions, would be affected. Accordingly, SNR predictions then need to include the effects of various analog and digital filters, the number of acquired samples, the noise covariance correction factor, and—most importantly—the non-central chi distribution of the noise statistics of the final magnitude image (Triantafyllou et al., 2011).

Another imaging parameter that affects the FRE but has not been further considered here is the slab thickness. Classically, a reduced slab thickness is associated with higher FRE due to a reduction in blood delivery time (Parker et al., 1991). However, this assumes that the vessel runs relatively straight through the imaging volume. This will not always hold true when imaging pial arteries, which have numerous right-angled branches and track the folding pattern of the cortex. In addition, blood velocities in larger arteries are much faster, and most of the blood delivery time can be assumed to be spent in the small branches, which would be included in both thicker and thinner slabs. Nevertheless, we have used comparatively thin slabs due to the long acquisition times and higher risk of motion that would be associated with larger imaging volumes. Future acquisitions might be able to

utilize the SNR increase from larger imaging volumes to increase acceleration and thus provide larger coverage at similar acquisition times.

In summary, numerous theoretical and practical considerations remain for optimal imaging of pial arteries using time-of-flight contrast. Depending on the application, advanced displacement artefact compensation strategies may be required, and zero-filling could provide better vessel depiction. Further, an optimal trade-off between SNR, voxel size and acquisition time needs to be found. Currently, the partial-volume FRE model only considers voxel size, and—as we reduced the voxel size in the experiments—we (partially) compensated the reduction in SNR through longer scan times. This, ultimately, also required the use of prospective motion correction to enable the very long acquisition times necessary for 140 µm isotropic voxel size. Often, anisotropic voxels are used to reduce acquisition time and increase SNR while maintaining in-plane resolution. This may indeed prove advantageous when the (also highly anisotropic) arteries align with the anisotropic acquisition, e.g. when imaging the large supplying arteries oriented mostly in the head-foot direction. In the case of pial arteries, however, there is not preferred orientation because of the convoluted nature of the pial arterial vasculature encapsulating the complex folding of the cortex (see section *Anatomical architecture of the pial arterial vasculature*). A further reduction in voxel size may be possible in dedicated research settings utilizing even longer acquisition times and/or larger acquisition volumes to maintain SNR. However, if acquisition time is limited, voxel size and SNR need to be carefully balanced against each other.

Challenges for vessel segmentation algorithms

The vessel segmentations presented here were performed to illustrate the sensitivity of the image acquisition to small pial arteries and are based on a simple combination of thresholding and region-growing. Thus, there is much potential for increased detection sensitivity and accuracy by employing more sophisticated approaches (Bernier et al., 2018; Chen et al., 2018; Frangi et al., 1998; Hsu et al., 2019, 2017; Lesage et al., 2009; Nowinski et al., 2011; Suri et al., 2002); Supplementary Figure 11 provides an example of this potential using manual segmentation on a small patch of the data presented in Figure 7. Given that the *manual* segmentation of these vessels is relatively simple, albeit arduous, machine learning approaches (Hilbert et al., 2020; Tetteh et al., 2020) also seem promising, as they commonly perform well in visual tasks (LeCun et al., 2015; Rueckert et al., 2016; Zaharchuk et al., 2018) and have successfully been applied to large-scale vasculature segmentations of mouse tissue-cleared data (Todorov et al., 2020). In general, the main challenges for these algorithms include the small vessel size compared to the voxel size, the broad range of vessel diameters, and the high noise levels.

Further, inflow in large pial veins and the dural venous sinuses can lead to high image intensities in these venous structures, and, consequently, false positives in the segmentation and identification of pial arteries. While additional radiofrequency pulses (Meixner et al., 2019; Schmitter et al., 2012) can be played out during image acquisition to suppress venous signal, the associated higher power deposition and increased acquisition times would reduce the imaging efficiency. Thus, we instead explored the removal of unwanted veins using a low-resolution two-echo TOF acquisition and T_2^* estimates to identify non-arterial vessels in the segmentation of the high-resolution data (Bae et al., 2010; Deistung et al., 2009; Du et al., 1994; Du and Jin, 2008).

The success of this vein removal approach hinges on two conditions: the quality of the segmentation, i.e. each segmented vessel is either an artery or a vein and no erroneous connections between the two classes arose during segmentation, and the assumption that venous vessels are present in both low- and high-resolution acquisitions. While the removal based on segmenting low-resolution data proved to be sufficient to demonstrate this approach (Figure 9), the segmentation of the high-resolution data suffered from a number of instances where veins and arteries were artifactually joined, and prohibited the full application of this technique to the native high-resolution data. Note the posterior lateral veins on both sides of the brain present in Figure 7, which require a higher exclusion threshold (see section Data Analysis) to prevent the removal of joined arteries and veins. Thus, utilizing the numerous possible improvements in the segmentation algorithm (see above), these segmentation errors can be prevented in the future to improve vein-removal for high-resolution data.

Our approach also assumes that the unwanted veins are large enough that they are also resolved in the low-resolution image. If we consider the source of the FRE effect and the type of vessels identified in Figure 9, it might indeed be exclusively large veins that are present in TOF-MRA data, which would suggest that our assumption is valid. Fundamentally, the FRE depends on the inflow of un-saturated spins into the imaging slab. However, small veins drain capillary beds in the local tissue, i.e. the tissue within the slab. (Note that due to the slice oversampling implemented in our acquisition, spins just above or below the slab will also be excited.) Thus, small pial veins only contain blood water spins that have experienced a large number of RF pulses due to the long transit time through the pial arterial vasculature, the intracortical arterioles, the capillaries and the intracortical venules. Accordingly, the blood delivery time for pial veins is much longer as it includes the blood delivery time for pial arteries, in addition to the blood transit time through the entire intracortical vasculature. Hence, their longitudinal magnetization would be similar to that of stationary tissue. To generate an FRE effect in veins, “pass-through” venous blood from outside the imaging slab is required. This is only available in veins that are passing through the imaging slab, which have much larger diameters. These

theoretical considerations are corroborated by the findings in Figure 9, where large disconnected vessels with varying intensity profiles were identified as non-arterial. Due to the heterogenous intensity profiles in large veins and the sagittal and transversal sinuses, the intensity-based segmentation applied here may only label a subset of the vessel lumen, creating the impression of many small veins. This is particularly the case for the straight and inferior sagittal sinus in the bottom slab of Figure 9. Nevertheless, future studies potentially combing anatomical prior knowledge, advanced segmentation algorithms and susceptibility measures would be capable of removing these unwanted veins in post-processing to enable an efficient TOF-MRA image acquisition dedicated to optimally detecting small arteries without the need for additional venous suppression RF pulses.

Once these challenges for vessel segmentation algorithms are addressed, a thorough quantification of the arterial vasculature can be performed. For example, the skeletonization procedure used to estimate the increase of the total length of the segmented vasculature (Supplementary Figure 9) exhibits errors particularly in the unwanted sinuses and large veins. While they are consistently present across voxel sizes, and thus may have less impact on relative change in skeleton length, they need to be addressed when estimating the absolute length of the vasculature, or other higher-order features such as number of new branches. (Note that we have also performed the skeletonization procedure on the maximum intensity projections to reduce the number of artefacts and obtained comparable results: reducing the voxel size from 0.8 mm to 0.5 mm isotropic increases the skeleton length by 44 % (3D) vs 37 % (2D), reducing the voxel size from 0.5 mm to 0.4 mm isotropic increases the skeleton length by 28 % (3D) vs 26 % (2D), reducing the voxel size from 0.4 mm to 0.3 mm isotropic increases the skeleton length by 31 % (3D) vs 16 % (2D), and reducing the voxel size from 0.16 mm to 0.14 mm isotropic increases the skeleton length by 14 % (3D) vs 24 % (2D).)

Computational simulations of blood flow based on these segmentations (Hsu et al., 2017; Park et al., 2020) also require accurate estimates of vessel diameter. However, when vessel diameter and voxel size are similar, diameter estimates often result in large relative errors (Hoogeveen et al., 1998; Klepaczko et al., 2016). One could imagine using the partial-volume model presented here (Eq. (4)) to correct for these partial volume effects (Nowinski et al., 2011) by modelling voxel intensities as a mixture of vessel and background intensities. However, this approach requires accurate knowledge of the blood delivery time to estimate the blood signal (Eq. (2)) and further neglects the fact that more than one tissue class typically surrounds pial vessels (see section *Anatomical architecture of the pial arterial vasculature* and Figure 1). In particular the different longitudinal relaxation times of grey matter and cerebrospinal fluid can generate distinct background intensities (Rooney et al., 2007; Wright et al., 2008). Additionally, the unknown position of the vessel within the voxel plays a significant role when determining the tissue and blood volume fractions, especially when voxel size

and vessel diameter are similar. In summary, advanced segmentation algorithms are needed to fully extract the information contained in these data, the removal of unwanted veins might be possible using an additional two-echo TOF acquisition, and vessel diameter estimates need to address potential large errors for vessels that are of similar diameter as the voxel size.

Future directions

The advantages of imaging the pial arterial vasculature using TOF-MRA without an exogenous contrast agent lie in its non-invasiveness and the potential to combine these data with various other structural and functional image contrasts provided by MRI. One common application is to acquire a velocity-encoded contrast such as phase-contrast MRA (Arts et al., 2021; Bouvy et al., 2016). Another interesting approach utilises the inherent time-of-flight contrast in magnetization-prepared two rapid acquisition gradient echo (MP2RAGE) images acquired at ultra-high field that simultaneously acquires vasculature and structural data, albeit at lower achievable resolution and lower FRE compared to the TOF-MRA data in our study (Choi et al., 2020). In summary, we expect high-resolution TOF-MRA to be applicable also for group studies to address numerous questions regarding the relationship of arterial topology and morphometry to the anatomical and functional organization of the brain, and the influence of arterial topology and morphometry on brain hemodynamics in humans. Notably, we have focused on imaging pial arteries of the human cerebrum; however, other brain structures such as the cerebellum, subcortex and white matter are of course also of interest. While the same theoretical considerations apply, imaging the arterial vasculature in these structures will require even smaller voxel sizes due to their smaller arterial diameters (Duvernoy et al., 1983, 1981; Nonaka et al., 2003a). In addition, imaging of the pial *venous* vasculature—using susceptibility-based contrasts such as T_2^*-weighted magnitude (Gulban et al., 2021) or phase imaging (Fan et al., 2015), susceptibility-weighted imaging (SWI) (Eckstein et al., 2021; Reichenbach et al., 1997) or quantitative susceptibility mapping (QSM) (Bernier et al., 2018; Huck et al., 2019; Mattern et al., 2019; Ward et al., 2018)—would enable a comprehensive assessment of the complete cortical vasculature and how both arteries and veins shape brain hemodynamics.

When applying measures of arterial topology and morphometry to address questions about the robustness of blood supply (Baumbach and Heistad, 1985), arterial territories (Mut et al., 2014) or the relationship between the cortical folding pattern and the pial vasculature (Ii et al., 2020), particular care needs to be exercised to account for the 'voxel size' bias. By this we mean that the dependency of the vessel contrast on the voxel size shown in our study in conjunction with the reduction in vessel diameter along the vascular tree (Duvernoy et al., 1981; Helthuis et al., 2019) can introduce a systematic detection bias that varies regionally. At lower imaging resolutions, we would expect particularly high numbers of false negatives for example in anterior and posterior brain regions, which

are the end points of the pial vascular tree and whose arteries generally have lower vessel diameters. This bias can lead to misinterpretations of the data such as an apparent reduction in vessel density, or an incorrect inference of slower blood flow in these regions. Further, anatomical modelling and vascular network synthesis methods rely on a detailed and unbiased description of the cerebral arterial vasculature to serve as a reference for the developed algorithms (Bui et al., 2010; Ii et al., 2020; Keelan et al., 2019). Finally, computational models of the pial arterial vasculature might be particularly relevant for future investigations into how the local vasculature shapes the spatio-temporal physiological and hemodynamic responses observed in BOLD and non-BOLD fMRI (Amemiya et al., 2020; Bright et al., 2020; Chen et al., 2020; Drew et al., 2020).

Estimating the sensitivity of TOF-MRA to pial vessels and verifying our finding that the voxel size is the determining factor for vessel depiction would arguably benefit from complementary imaging methods such as optical coherence tomography, which provides superior sensitivity and specificity for small pial vessel (Baran and Wang, 2016). These techniques are commonly used in rodents, but because of their limited penetration depth however, not in humans. Notably, blood velocity measurements can also be obtained (Wang and An, 2009; You et al., 2014) allowing a direct estimate of blood delivery time to delineate the impact of voxel size and blood delivery time on FRE (Figure 4).

In summary, when imaging the pial arterial vasculature we found that—unexpectedly—the limiting factor is not the vascular “physiology”, i.e. not slow blood flow in pial arteries, but rather the currently available image resolution. This new perspective provides further motivation to push to higher imaging resolutions, which will provide an even more detailed picture of the pial arterial network. While many challenges remain to obtain high-quality high-resolution images and vascular segmentations, we expect the techniques presented here to allow new insights into the topology and morphometry of the pial arterial vasculature. Given the stark improvements in vessel contrast when using smaller voxels, we believe that as imaging technology progresses, faster and higher-resolved acquisition techniques will become available. Utilizing the potential of higher field strengths, advanced receive coil arrays, new reconstruction techniques, faster imaging gradients and sophisticated motion correction will enable broad applications of this approach to both basic neuroscience and clinical research.

Methods

Simulations

The simulations of the FRE as a function of sequence parameter (Figure 4, Eq. (1)–Eq. (3)) or voxel size and blood delivery time (Figure 5, Eq. (4)–Eq. (6)) were performed in Matlab R2020a (The MathWorks, Natick, MA) and are available online: https://gitlab.com/SaskiaB/pialvesseltof.git (branch: paper-version). The calculation of the relative blood volume (Eq. (4)) to estimate the partial-volume FRE (Eq. (6)) is outlined in the supplementary material (*Estimation of vessel-volume fraction*). Where not stated otherwise, simulations were performed assuming a pial artery diameter of 200 µm, a T_R value of 20 ms, an excitation flip angle of 18°, a blood delivery time of 400 ms, and longitudinal relaxation times of blood and tissue of 2100 ms and 1950 ms at 7 T, respectively (Huber, 2014, Table 2.1).

Data acquisition

Four healthy adults volunteered to participate in the study (four males, ages 30-46). Prior to imaging, written informed consent was obtained from each participant in accordance with the Partners Human Research Committee and the Massachusetts General Hospital Institutional Review Board (Figure 5, 6, 8 and 9 and Supplementary Figure 4, 5, 6 and 9) and the 'Ethikkommission Otto-von-Guericke-Universität Magdeburg' (Figure 7 and Supplementary Figure 7, 8 and 11). Experiments were conducted at 7T on a Siemens MAGNETOM whole-body scanner (Siemens Healthcare, Erlangen, Germany) equipped with SC72 gradients. Imaging data presented in Figure 5, 6, 8 and 9 and Supplementary Figure 4, 5 and 6 were acquired at the Athinoula A. Martinos Center for Biomedical Imaging, Massachusetts General Hospital, Boston, using an in-house built head-only birdcage volume transmit coil and 31-channel receive coil array. Imaging data the presented in Figure 7 and Supplementary Figure 7, 8, 9 and 11 were acquired at the Institute of Experimental Physics, Otto-von-Guericke-University, Magdeburg using a quadrature transmit and 32-channel receive head coil (Nova Medical, Wilmington, Massachusetts, USA) and an optical, marker-based tracking system with an in-bore camera (Metria Innovation, Milwaukee, Wisconsin, USA) for prospective motion correction.

To empirically assess the effect of resolution on FRE, the vendor-supplied TOF sequence was utilized to acquire MRA data at 0.3 mm, 0.4 mm, 0.5 mm and 0.8 mm isotropic resolution. For each resolution all other sequence parameters were kept as identical as possible: T_E = 4.73 ms with asymmetric echo, T_R = 20 ms, flip angle = 18°, FOV = 204 mm × 178.5 mm, slab thickness = [21.6 mm, 19.2 mm, 22 mm, 25.6 mm], slice oversampling = [22 %, 25 %, 18.2 %, 12.5 %], R ≫ L phase encoding direction, readout bandwidth = 120 Hz/px, GRAPPA (Griswold et al., 2002) = 3, number of reference lines = 32, no partial Fourier, 3D centric reordering of the phase encoding steps (Korin et al., 1992), read and slab-select flow compensation (Parker et al., 2003) resulting in a total acquisition time of 6 min 42 s, 3 min 29 s, 2 min 23 s and 1 min 14 s, respectively. Note that the employed flow

compensation only accounts for signal loss due to the readout and slab-select gradients, but not for potential vessel displacements in the phase-encoding directions. Tilt-optimized, nonsaturated excitation (TONE) pulses (Atkinson et al., 1994), which are commonly employed to obtain a homogenous image contrast (Atkinson et al., 1994; Carr and Carroll, 2012; Nägele et al., 1995), were not used; because these dedicated RF pulses are most effective when blood flow is perpendicular to the imaging slab and moving in the direction of the TONE pulse ramp, e.g. in the H ≫ F direction. However, in the case of pial arteries the complex branching pattern of the vasculature on the folded cortex means that no preferential flow direction is present. Thus, the optimal direction of the TONE ramp is undetermined and therefore this technique is not appropriate for imaging the mesoscopic pial arteries.

The high-resolution TOF acquisitions used the same vendor-supplied TOF sequence, but with one slight modification to allows for larger image encoding matrices. The parameters for the TOF acquisition at 0.16 mm isotropic resolution (Figure 6 and Supplementary Figure 4) were the following: T_E = 6.56 ms with asymmetric echo, T_R = 20 ms, flip angle = 18°, FOV = 204 mm × 173.8 mm, slab thickness = 8.32 mm, slice oversampling = 15.4 %, R ≫ L phase encoding direction, readout bandwidth = 100 Hz/px, GRAPPA = 2, number of reference lines = 32, no partial Fourier, 3D centric reordering of the phase encoding steps, flow compensation in the read and slab-select directions, resulting in a total acquisition time of 11 min 42 s per slab. Immediately after each scan, the resulting images were visually inspected for motion artefacts, which manifest as a loss of image sharpness, and feedback was provided to the participant about their performance. If motion was detected, the scan was repeated. To cover a larger area, the imaging slab was moved head-foot following each scan and the acquisition was repeated after ensuring that the participant was still comfortable.

The high-resolution TOF acquisition at 0.14 mm isotropic resolution (Figure 5 and Supplementary Figure 7, 8, 9 and 11) utilized a prospective motion correction system to enable longer scan times and minimize the effect of subject motion. We followed the procedure described in Mattern et al. (2018). In brief, a 15 × 15 mm^2 marker with a Morié pattern was attached via an individually made mouthpiece to the subject's teeth, skull and thus brain (Callaghan et al., 2015). A camera, which tracked the marker at 80 frames per second, was positioned above the subject's head in the scanner. The rigid-body motion parameters estimated from the video stream were sent to the MRI scanner to update the imaging volume every T_R. In total, 3 imaging slabs were acquired in 1 h 5 min 40 s covering 19.6 mm in the head-foot direction. The following pulse sequence parameters were used: T_E = 6.99 ms with asymmetric echo, T_R = 20 ms, flip angle = 18°, FOV = 204 mm × 153 mm, slab thickness = 7.28 mm, slice oversampling = 15.4 %, R ≫ L phase encoding direction, readout bandwidth = 100 Hz/px, no parallel imaging, no partial Fourier, 3D centric reordering of the phase

encoding steps, read and slab-select flow compensation resulting in a total acquisition time of 21 min 53 s per slab. For comparison, a single slab at 0.16 mm isotropic resolution with the same pulse sequence parameters described in the previous paragraph was acquired.

To assess the magnitude of the vessel displacement artefact (Figure 8) and verify the feasibility of unwanted vein removal during post-processing (Figure 9) (Deistung et al., 2009; Du and Jin, 2008), we acquired additional two-echo TOF data in a fourth participant with the following parameters: isotropic voxel size = 0.4 mm, T_E = [7.05 ms, 14 ms] with asymmetric echo, T_R = 20 ms, flip angle = 18°, FOV = 204 mm x 153 mm, slab thickness = 20.8 mm, number of slabs = 4, slice oversampling = 23.1 %, R ≫ L phase encoding direction, readout bandwidth = 200 Hz/px, monopolar readout, GRAPPA = 4, no partial Fourier, no 3D centric reordering of the phase encoding steps, full gradient-moment based flow compensation in read and phase encoding directions resulting in a total acquisition time of 10 min 42 s.

The anonymized imaging data presented in this manuscript are stored in OSF (OSF, Center for Open Science, Inc., Charlottesville, Virginia, USA) accessible via https://osf.io/nr6gc/. Note that additional multi-contrast high-resolution imaging data are available from this participant (Lüsebrink et al., 2021, 2017). Within the OSF repository, high-resolution versions of the figures contained in this manuscript are also provided.

Data analysis

All imaging data were slab-wise bias-field corrected using the *N4BiasFieldCorrection* (Tustison et al., 2010) tool in ANTs (Avants et al., 2009) with the default parameters. To compare the empirical FRE across the four different resolutions (Figure 5), manual masks were first created for the smallest part of the vessel in the image with the highest resolution and for the largest part of the vessel in the image with the lowest resolution. Then, rigid-body transformation parameters from the low-resolution to the high-resolution (and the high-resolution to the low-resolution) image were estimated using *coregister* in SPM (https://www.fil.ion.ucl.ac.uk/spm/), and their inverse was applied to the vessel mask using SPM's *reslice*. To calculate the empirical FRE (Eq. (3)), the mean of the intensity values within the vessel mask was used to approximate the blood magnetization, and the mean of the intensity values one voxel outside of the vessel mask was used as the tissue magnetization.

For vessel segmentation, a semi-automatic segmentation pipeline was implemented in Matlab R2020a (The MathWorks, Natick, MA) using the UniQC toolbox(Frässle et al., 2021): First, a brain mask was created through thresholding which was then manually corrected in ITK-SNAP (http://www.itksnap.org/) (Yushkevich et al., 2006) such that pial vessels were included. For the high-resolution TOF data (Figure 6 and 7, Supplementary Figure 4), denoising to remove high frequency noise was performed using the implementation of an adaptive non-local means denoising algorithm

(Manjón et al., 2010) provided in *DenoiseImage* within the ANTs toolbox, with the search radius for the denoising set to 5 voxels and noise type set to Rician. Next, the brain mask was applied to the bias corrected and denoised data (if applicable). Then, a vessel mask was created based on a manually defined threshold, and clusters with less than 10 or 5 voxels for the high- and low-resolution acquisitions, respectively, were removed from the vessel mask. Finally, an iterative region-growing procedure starting at each voxel of the initial vessel mask was applied that successively included additional voxels into the vessel mask if they were connected to a voxel which was already included and above a manually defined threshold (slightly below the previous threshold). Both thresholds were applied globally but manually adjusted for each slab. No correction for motion between slabs was applied. The Matlab code describing the segmentation algorithm as well as the analysis of the two-echo TOF acquisition outlined in the following paragraph are also included in our github repository (https://gitlab.com/SaskiaB/pialvesseltof.git). To estimate the increased detection of vessels with higher resolutions, we computed the relative increase in the length of the segmented vessels for the data presented in Figure 5 (0.8 mm, 0.5 mm, 0.4 mm and 0.3 mm isotropic voxel size) and Figure 7 (0.16 mm and 0.14 mm isotropic voxel size) by computing the skeleton using the *bwskel* Matlab function and then calculating the skeleton length as the number of voxels in the skeleton multiplied by the voxel size.

The stronger background signal in the lower-resolution two-echo TOF acquisition necessitated a more advanced vessel segmentation algorithm. We therefore utilized the procedure described in Bernier et al. (2018) to derive the initial vessel mask, before performing the region-growing procedure. To illustrate the vessel displacement, segmentation of the second echo was skeletonized using the *bwskel* Matlab function, which was then overlaid on the MIP of the first echo (Figure 8) to highlight the vessel centerline shift between the two echoes. The voxel-wise T_2^* values for the vein removal were estimated from the natural logarithm of the intensity ratios of the two echoes and the echo time difference. Vessels were deemed to be unwanted veins if the 90 % percentile of the T_2^* values in each independent (unconnected) vessel/vessel tree was below 19 ms (Figure 9) or 27 ms (Figure 7).

To estimate the vessel density mentioned in the *Anatomical architecture of the pial arterial vasculature* section, the drawing in Figure 239 in Duvernoy (1999) was segmented into arteries, veins and background using their RGB values to estimate their relative content.

Supplementary material

Estimation of vessel-volume fraction

To estimate the relative blood-volume fraction $V_{\text{blood}}^{\text{rel}} = V_{\text{vesselInVoxel}}/V_{\text{voxel}}$, we assume a centrally located vessel with radius r_{vessel} in a voxel with equal length l_{voxel} along each side. The vessel cross-sectional area, orthogonal to the main axis of the vessel and intersecting the voxel, is split into 8 equal areas A, as indicated in Supplementary Figure 1. The relative blood volume fraction $V_{\text{blood}}^{\text{rel}}$ can then be computed as the sum of these 8 compartments times the voxel length l_{voxel} relative to the voxel volume:

$$V_{\text{blood}}^{\text{rel}} = \frac{8 \cdot A \cdot l_{\text{voxel}}}{V_{\text{voxel}}} \qquad \text{Eq. (8)}$$

If $l_{\text{voxel}} < \cos\frac{\pi}{2} \cdot r_{\text{vessel}}$ (case I), i.e. the voxel is completely contained in the vessel, the total vessel area in the voxel is

$$A_{\text{case I}} = \frac{1}{2} \cdot \left(\frac{l_{\text{voxel}}}{2}\right)^2. \qquad \text{Eq. (9)}$$

Conversely, if $r_{\text{vessel}} < l_{\text{voxel}}/2$ (case III), i.e. the vessel is completely contained in the voxel, the total vessel area in the voxel is

$$A_{\text{case III}} = \frac{1}{2} \cdot r_{\text{vessel}}^2 \cdot \frac{\pi}{4}. \qquad \text{Eq. (10)}$$

In the case when vessel and voxel intersect, the total area A is the sum of the area A' of the right triangle and area A'' of the circular sector:

$$\begin{aligned} A_{\text{case II}} &= A' + A'' \\ A' &= \frac{1}{2} \cdot a \cdot \frac{l_{\text{voxel}}}{2} \\ a &= \sin\theta \cdot r_{\text{vessel}} \\ \theta &= \cos^{-1}\frac{\frac{l_{\text{voxel}}}{2}}{r_{\text{vessel}}} \\ A'' &= \frac{1}{2} \cdot r_{\text{vessel}}^2 \cdot \left(\frac{\pi}{4} - \theta\right) \end{aligned} \qquad \text{Eq. (11)}$$

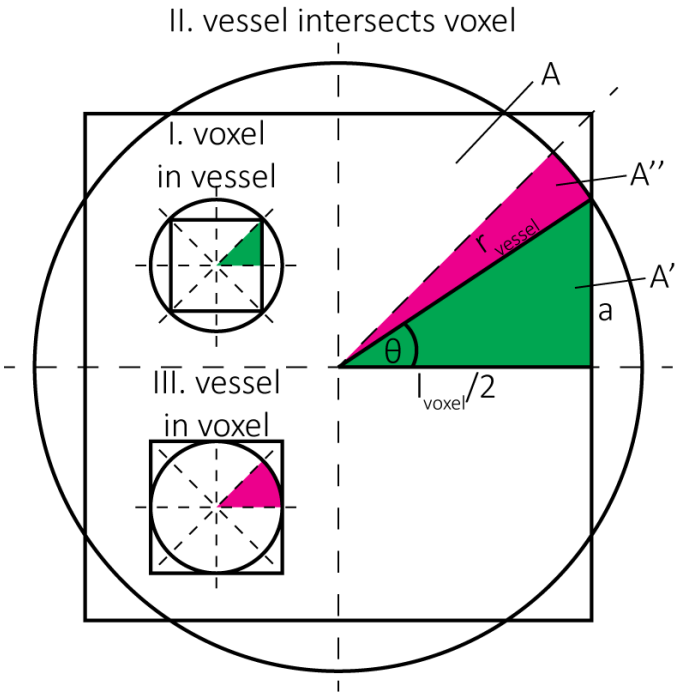

Supplementary Figure 1: Estimation of the blood volume fraction for case (I) voxel in vessel, case (II) vessel intersects voxel and case (III) vessel in voxel. The pink regions indicate circular sectors and the green regions indicate right triangles. The full split into the 8 equal areas A is shown for case (I) and (III), the partial areas A' and A'' are shown for case (II).

Effect of FRE Definition and Interaction with Partial-Volume Model

For the definition of the FRE effect in this study, we used a measure of relative FRE (Al-Kwifi et al., 2002) in combination with a partial-volume model (Eq. (6)). To illustrate the effect of these two definitions, as well as their interaction, we have estimated the relative and absolute FRE for an artery with a diameter of 200 µm and 2 000 µm (i.e. no partial-volume effects). The absolute FRE explicitly takes the voxel volume into account, i.e. instead of Eq. (6) for the relative FRE we used

$$FRE_{PV}(n_{RF},\, l_{voxel},\, d_{vessel}) = M_z^{total}(n_{RF},\, l_{voxel},\, d_{vessel}) \cdot l_{voxel}^3 - M_{zS}^{tissue} \cdot \left(l_{voxel}^3\right) \qquad \text{Eq. (12)}$$

Note that the division by $M_{zS}^{tissue} \cdot l_{voxel}^3$ to obtain the relative FRE removes the contribution of the total voxel volume $\left(l_{voxel}^3\right)$.

Supplementary Figure 2 shows that, when partial volume effects are present, the highest relative FRE arises in voxels with the same size as or smaller than the vessel diameter (Supplementary Figure 2A), whereas the absolute FRE increases with voxel size (Supplementary Figure 2C). If no partial-volume effects are present, the relative FRE becomes independent of voxel size (Supplementary Figure 2B), whereas the absolute FRE increases with voxel size (Supplementary Figure 2D). While the partial-volume effects for the relative FRE are substantial, they are much more subtle when using the absolute FRE and do not alter the overall characteristics.

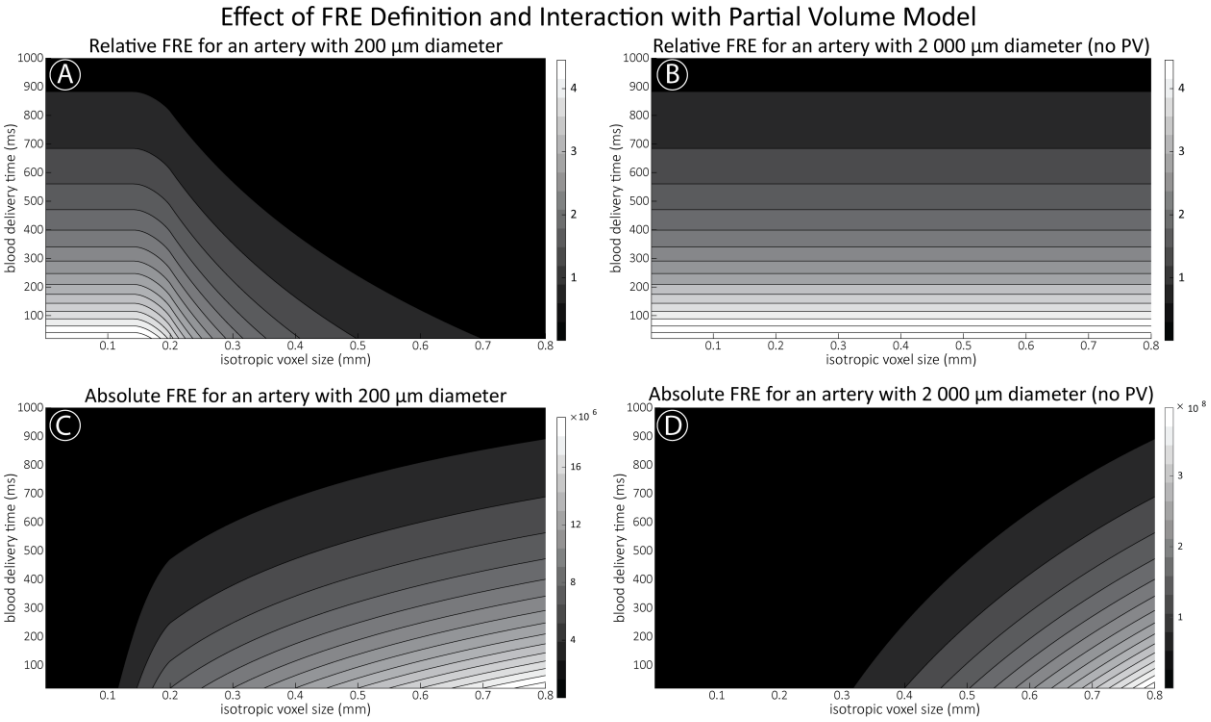

Supplementary Figure 2: Effect of voxel size and blood delivery time on the relative flow-related enhancement (FRE) using either a relative (A,B) (Eq. (3)) or an absolute (C,D) (Eq. (12)) FRE definition assuming a pial artery diameter of 200 µm (A,C) or 2 000 µm, i.e. no partial-volume effects at the central voxel of this artery considered here.

Optimization of repetition time and excitation flip angle

As the main goal of the optimisation here was to start within an already established parameter range for TOF imaging at ultra-high field (Kang et al., 2010; Stamm et al., 2013; von Morze et al., 2007), we only needed to then further tailor these for small arteries by considering a third parameter, namely the blood delivery time. From a practical perspective, a T_R of 20 ms as a reference point was favourable, as it offered a time-efficient readout minimizing wait times between excitations but allowing low encoding bandwidths to maximize SNR. Due to the interdependency of flip angle and repetition time, for any *one* blood delivery time any FRE could (in theory) be achieved. For example, a similar FRE curve at 18 ° flip angle and 5 ms T_R can also be achieved at 28 ° flip angle and 20 ms T_R; or the FRE curve at 18 ° flip angle and 30 ms T_R is comparable to the FRE curve at 8 ° flip angle and 5 ms T_R (Supplementary Figure 3 TOP). In addition, the difference between optimal parameter settings diminishes for long blood delivery times, such that at a blood delivery time of 500 ms (Supplementary Figure 3 BOTTOM), the optimal flip angle at a T_R of 15 ms, 20 ms or 25 ms would be 14 °, 16 ° and 18 °, respectively. This is in contrast to a blood delivery time of 100 ms, where the optimal flip angles would be 32 °, 37 ° and 41 °. In conclusion, in the regime of small arteries, long T_R values in combination with low flip angles ensure flow-related enhancement at blood delivery times of 200 ms and above, and within this regime there are marginal gains by further optimizing parameter values and the optimal values are all similar.

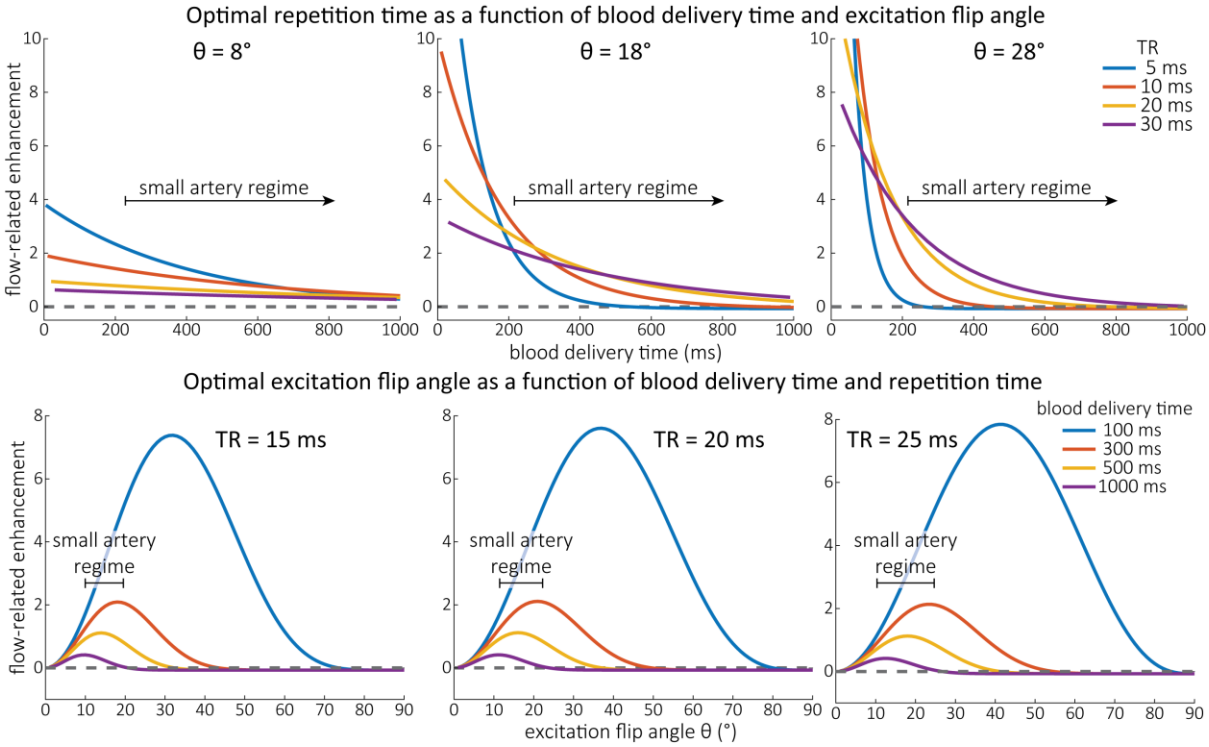

Supplementary Figure 3: Optimal imaging parameters for small arteries. This assessment follows the simulations presented in Figure 3, but in addition shows the interdependency for the corresponding third parameter (either flip angle or repetition time). TOP: Flip angles close to the Ernst angle show only a marginal flow-related enhancement; however, the influence of the blood delivery time decreases further (LEFT). As the flip angle increases well above the values used in this study, the flow-related enhancement in the small artery regime remains low even for the longer repetition times considered here (RIGHT). BOTTOM: The optimal excitation flip angle shows reduced variability across repetition times in the small artery regime compared to shorter blood delivery times.

Imaging of the pial arterial vasculature

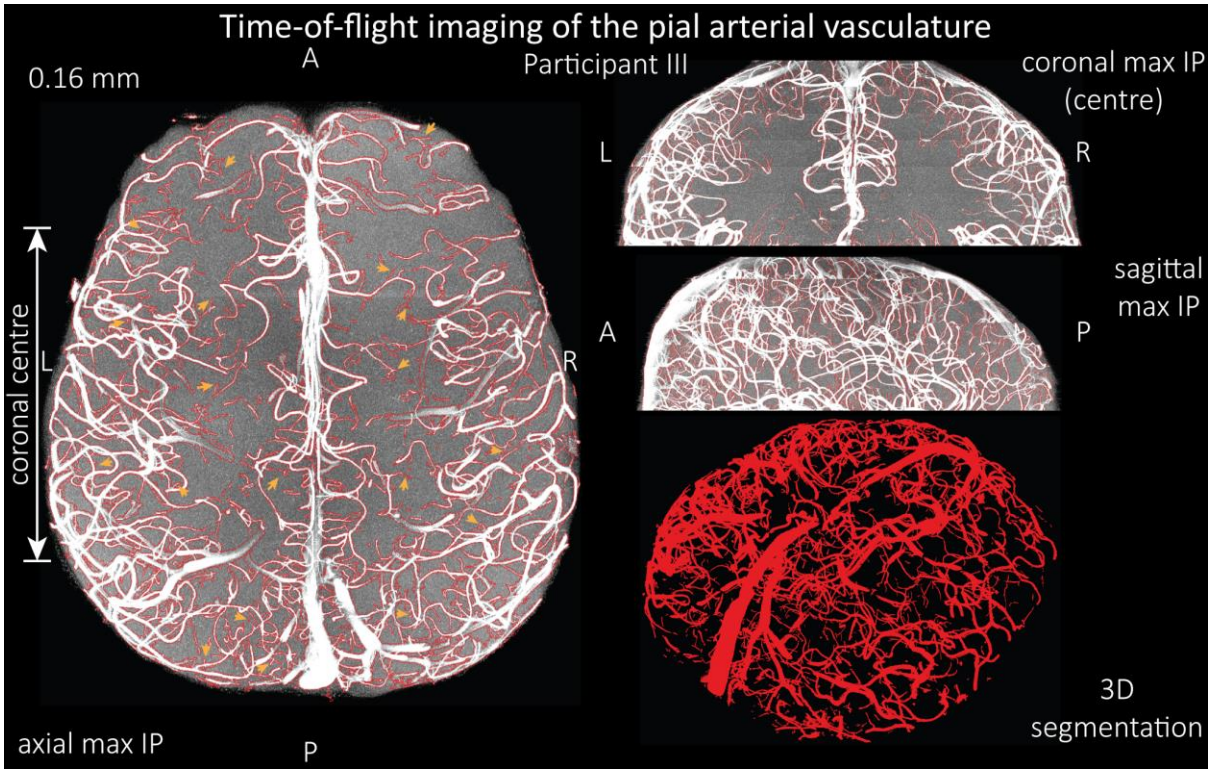

Supplementary Figure 4: Time-of-flight imaging of the pial arterial vasculature at 0.16 mm isotropic resolution and 58 mm coverage in the head-foot direction showing the results from participant III using the same acquisition protocol as for Figure 6. LEFT: Axial maximum intensity projection and outline of the vessel segmentation overlaid in red. Examples of the numerous right-angled branches are indicated by orange arrows. RIGHT: Coronal maximum intensity projection and segmentation of the central part of the brain (top), sagittal maximum intensity projection and segmentation (middle), and 3D view of the vessel segmentation (bottom).

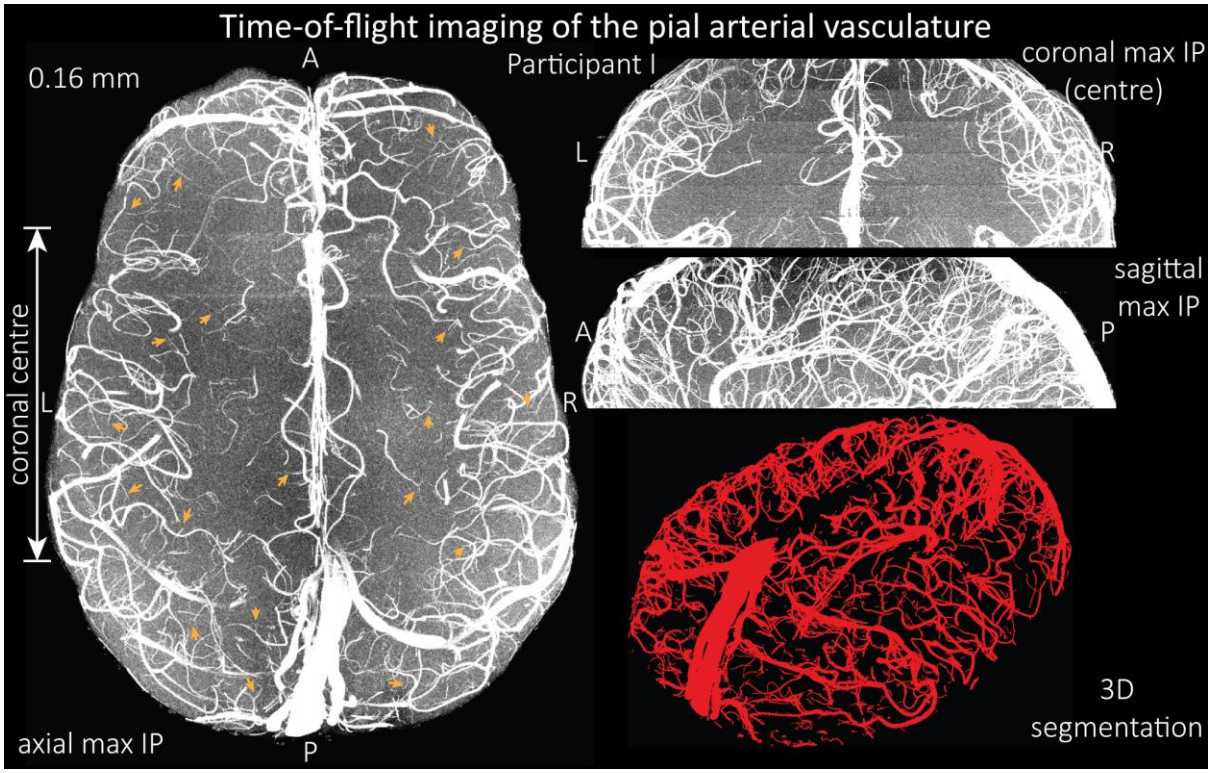

Supplementary Figure 5: Time-of-flight imaging of the pial arterial vasculature at 0.16 mm isotropic resolution and 50-mm coverage in the head-foot direction showing the same data of participant I as in Figure 6, but without the overlay of the segmentation. LEFT: Axial maximum intensity projection. Examples of the numerous right-angled branches are indicated by orange arrows. RIGHT: Coronal maximum intensity projection of the central part of the brain (TOP), sagittal maximum intensity projection (MIDDLE), and 3D view of the vessel segmentation (BOTTOM).

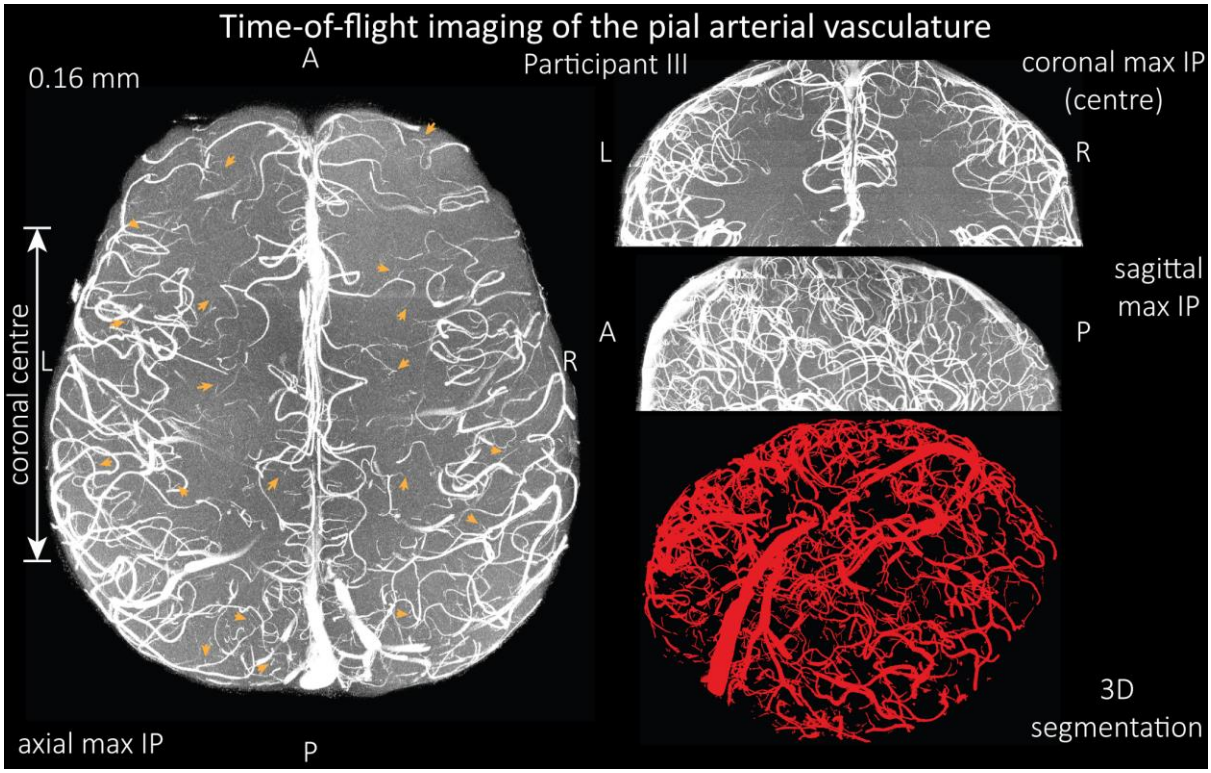

Supplementary Figure 6: Time-of-flight imaging of the pial arterial vasculature at 0.16 mm isotropic resolution and 58 mm-coverage in the head-foot direction showing the same data of participant III as in Supplementary Figure 4 but without the overlay of the segmentation. LEFT: Axial maximum intensity projection. Examples of the numerous right-angled branches are indicated by orange arrows. RIGHT: Coronal maximum intensity projection of the central part of the brain (TOP), sagittal maximum intensity projection (MIDDLE), and 3D view of the vessel segmentation (BOTTOM).

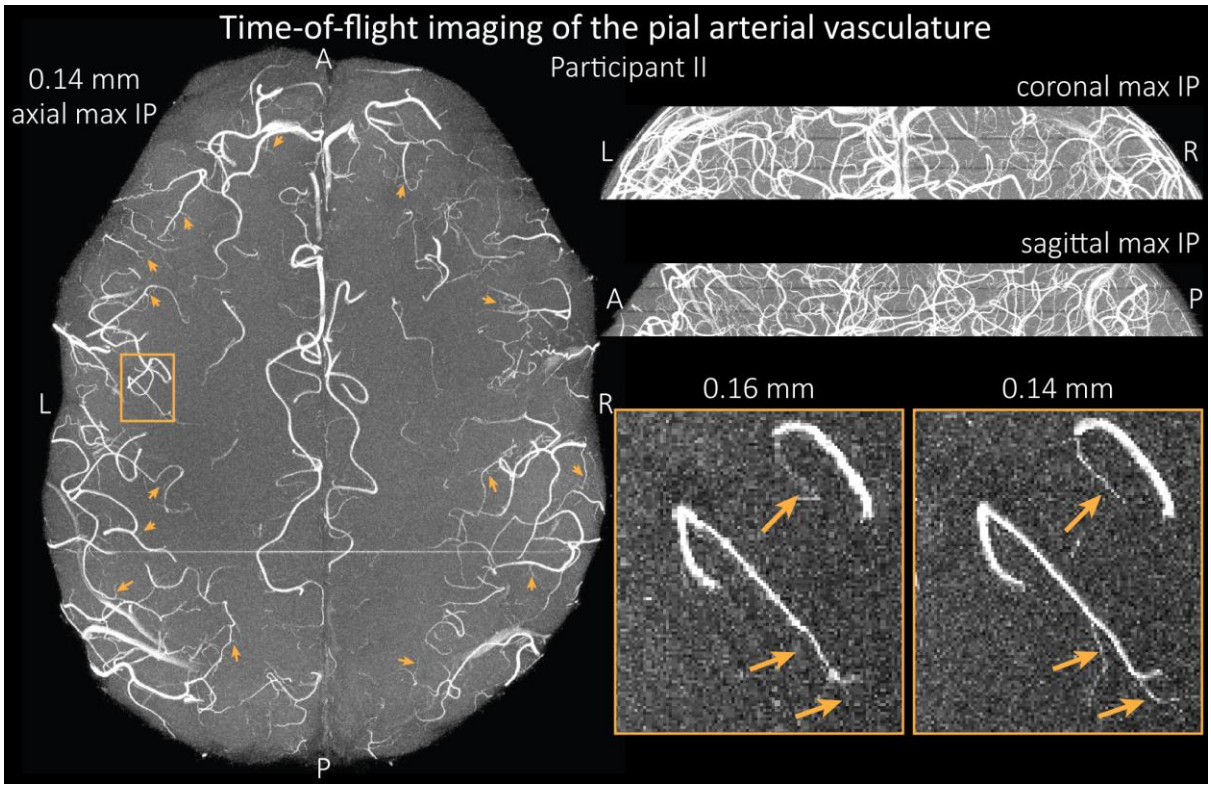

Supplementary Figure 7: Time-of-flight imaging of the pial arterial vasculature at 0.14 mm isotropic resolution and 19.6-mm coverage in the foot-head direction showing the same data of participant II as in Figure 7, but without the overlay of the segmentation. LEFT: Axial maximum intensity projection. Examples of the numerous right-angled branches are indicated by orange arrows. RIGHT: Coronal maximum intensity projection (TOP) and sagittal maximum intensity projection (MIDDLE). A comparison of 0.16 mm and 0.14 mm voxel size (BOTTOM) shows several vessels visible only at the higher resolution. The location of the insert is indicated on the axial maximum intensity projection on the left. Note that for this comparison the coverage of the 0.14 mm data was matched to the smaller coverage of the 0.16 mm data.

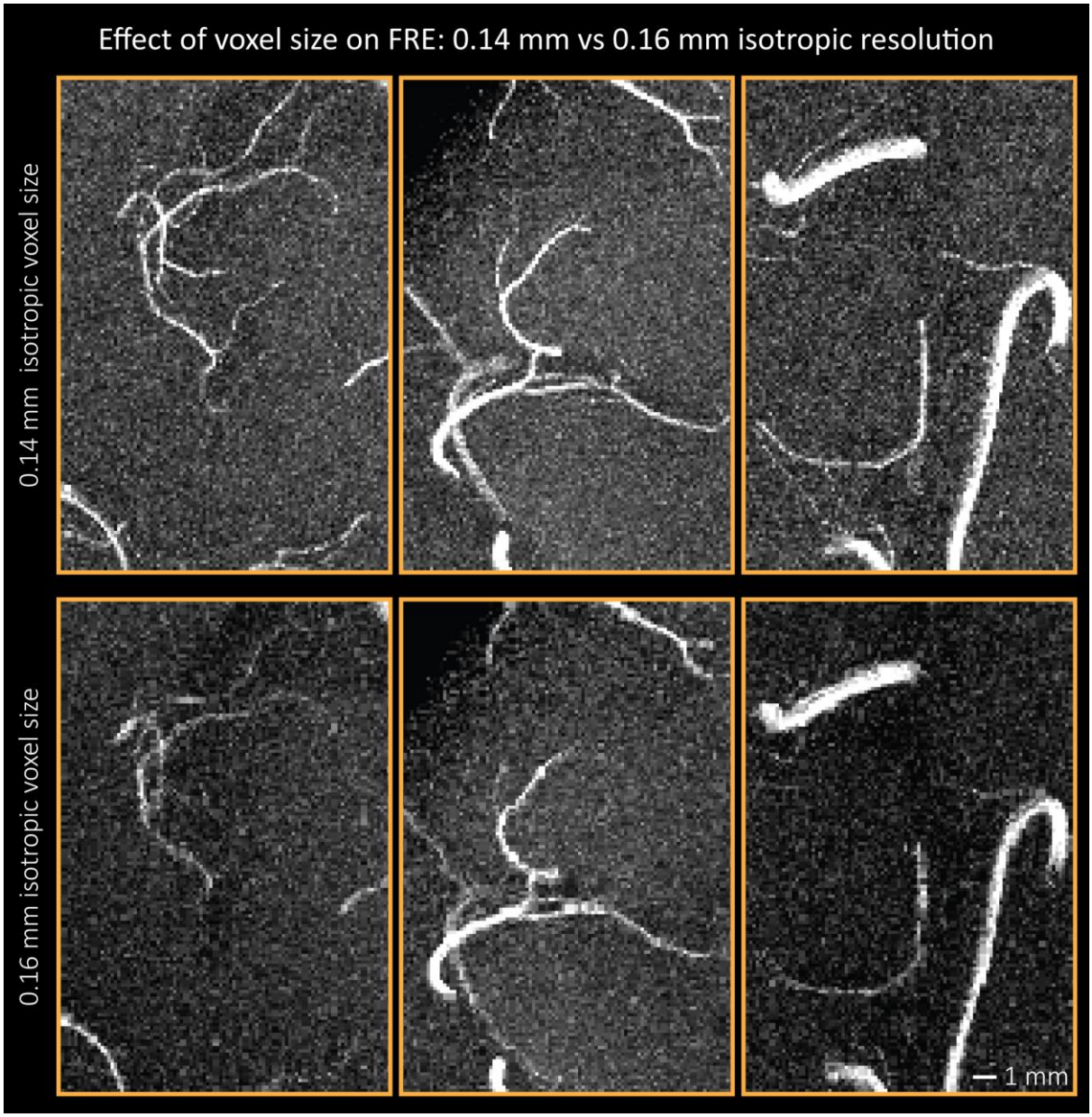

Supplementary Figure 8: Additional examples comparing the flow-related enhancement at 0.14 mm (TOP) and 0.16 mm (BOTTOM) voxel size showing additional small branches visible only at the higher resolution.

Increase in skeleton length

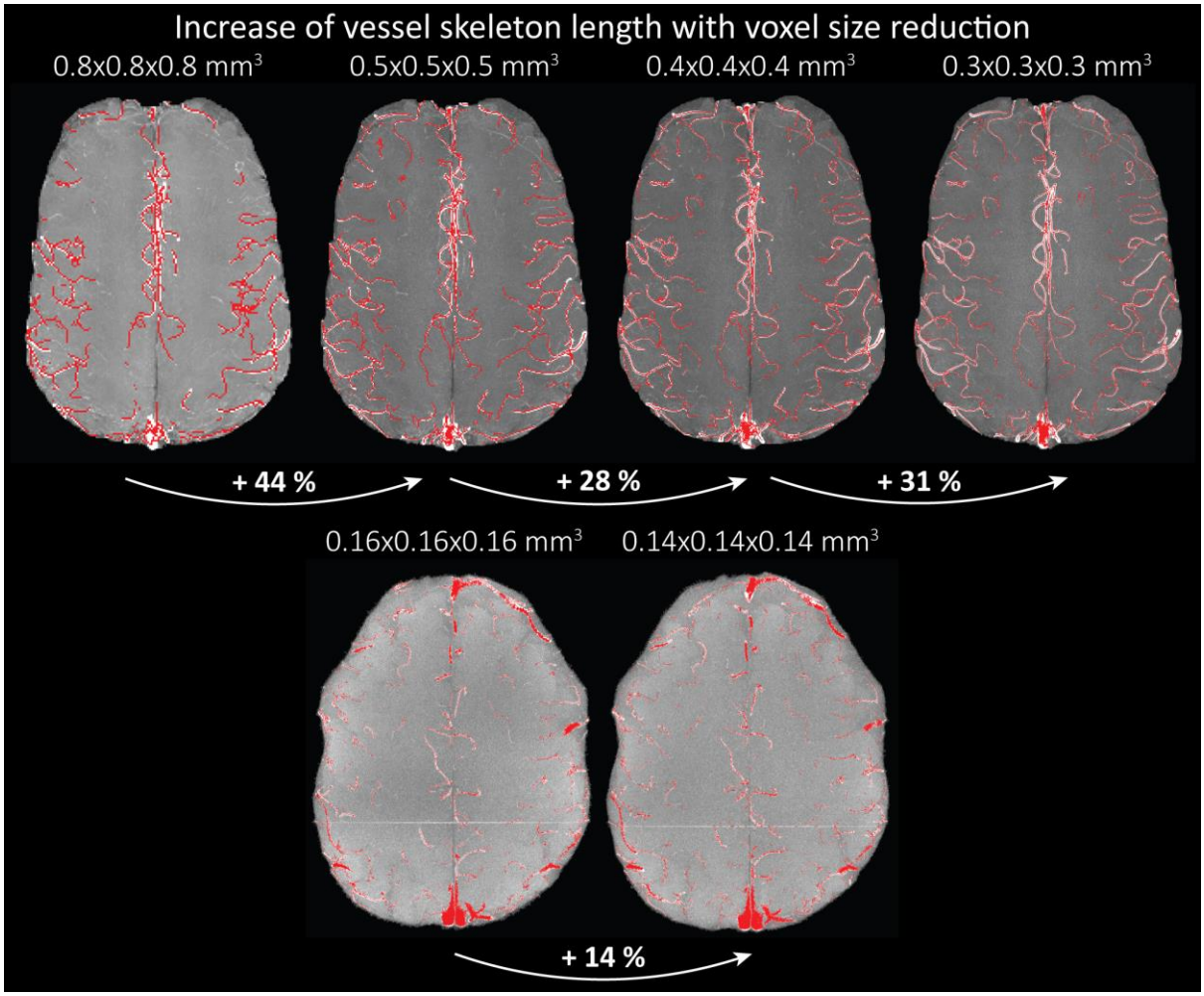

Supplementary Figure 9: Increase of vessel skeleton length with voxel size reduction. Axial maximum intensity projections for data acquired with different voxel sizes ranging from 0.8 mm to 0.3 mm (TOP) (corresponding to Figure 5) and 0.16 mm to 0.14 mm isotropic (corresponding to Figure 7) are shown. Vessel skeletons derived from segmentations performed for each resolution are overlaid in red. A reduction in voxel size is accompanied by a corresponding increase in vessel skeleton length.

Vessel displacement artefact

The origin of the vessel displacement artefact described in section *Inflow-artefacts in sinuses and pial veins*

Inflow in large pial veins and the sagittal and transverse sinuses can cause flow-related enhancement in these non-arterial vessels. One common strategy to remove this unwanted signal enhancement is to apply venous suppression pulses during the data acquisition, which saturate bloods spins outside the imaging slab. Disadvantages of this technique are the technical challenges of applying these pulses at ultra-high field due to constraints of the specific absorption rate (SAR) and the necessary increase in acquisition time (Conolly et al., 1988; Heverhagen et al., 2008; Johst et al., 2012; Maderwald et al., 2008; Schmitter et al., 2012; Zhang et al., 2015). In addition, optimal positioning of the saturation slab in the case of pial arteries requires further investigation, and in particular supressing signal from the

superior sagittal sinus without interfering in the imaging of the pial arteries vasculature at the top of the cortex might prove challenging. Furthermore, this venous saturation strategy is based on the assumption that arterial blood is traveling head-wards while venous blood is drained foot-wards. For the complex and convoluted trajectory of pial vessels this directionality-based saturation might be oversimplified, particularly when considering the higher-order branches of the pial arteries and veins on the cortical surface.

Inspired by techniques to simultaneously acquire a TOF image for angiography and a susceptibility-weighted image for venography (Bae et al., 2010; Deistung et al., 2009; Du et al., 1994; Du and Jin, 2008), we set out to explore the possibility of removing unwanted venous structures from the segmentation of the pial arterial vasculature during data postprocessing. Because arteries filled with oxygenated blood have $T2^*$-values similar to tissue, while veins have much shorter $T2^*$-values due to the presence of deoxygenated blood (Pauling and Coryell, 1936; Peters et al., 2007; Uludağ et al., 2009; Zhao et al., 2007), we used this criterion to remove vessels with short $T2^*$ values from the segmentation (see *Data Analysis* for details). In addition, we also explored whether unwanted venous structures in the high-resolution TOF images—where a two-echo acquisition is not feasible due to the longer readout—can be removed based on detecting them in a lower-resolution image.

Velocity- and TE-dependent vessel displacement artifacts and shown in Figure 8 is illustrated in Supplementary Figure 10A (Brown et al., 2014b). In short, the moving blood water spins accumulate the phase increment at time t_{pe} at position (x_{tpe}, y_{tpe}) encoding their position in the phase encoding direction y, but continue to flow along the blood vessel such that at the echo time (T_E) they are in position (x_{tTE}, y_{tTE}). Consequently, during image reconstruction the signal from these spins is located in position (x_{tTE}, y_{tpe}) which they have never occupied. The magnitude of the vessel displacement is simply the distance travelled by the blood water spins in the time between the phase-encoding blip and the echo time, and can be described as in equation Eq. (7) assuming a constant blood velocity. Supplementary Figure 10B illustrates that an inversion of the polarity of the phase encoding direction, a technique commonly used to estimate and correct for voxel displacements found in echo-planar imaging stemming from main magnetic field inhomogeneities (Andersson et al., 2003; Jezzard and Clare, 1999), does *not* change the direction of the displacement. This is because the vessel displacement is caused by true object motion, and while an inversion of the polarities would (in this example) imprint the 'correct' larger phase increment on the blood water spins from Panel A, this phase increment is now also associated with the inverted position and thus the vessel displacement occurs in the same direction.

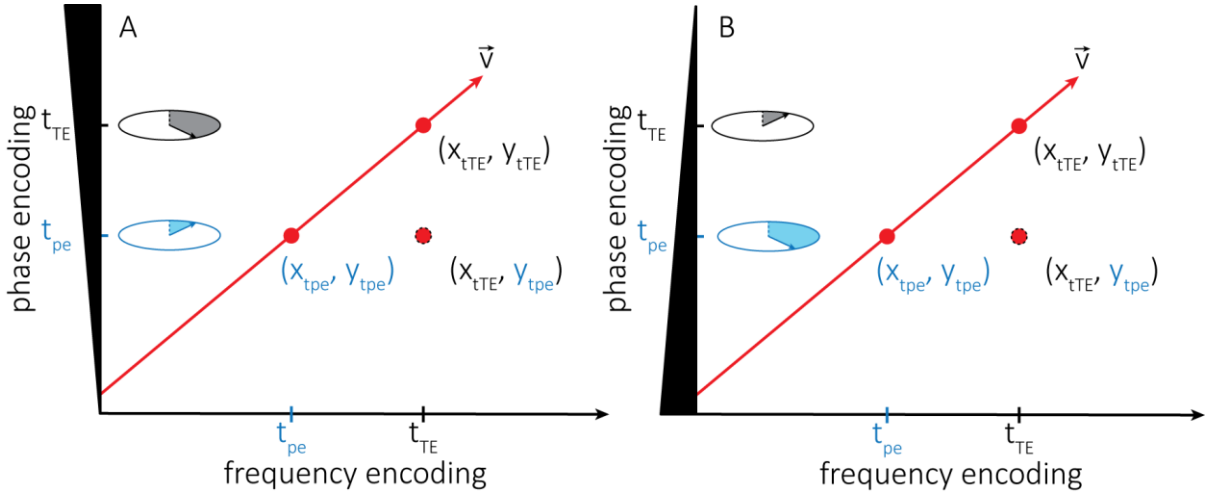

Supplementary Figure 10: (A) Illustration of the vessel displacement artefact in 2D caused by moving blood water spins. The blood water spins travel along the path indicated by the red arrow with velocity v and occupy different locations at the time of the phase-encoding blip (t_{pe}) and the echo time (t_{TE}). The resulting image location is a combination of their position at time t_{pe} in the phase encoding direction y and their position at time t_{TE} in the frequency encoding direction x. (B) Describes the same process but with the inverted polarity of the phase encoding gradient.

Potential for advanced segmentations algorithms

The potential for advanced segmentation algorithms is illustrated in Supplementary Figure 11, where a small section of the time-of-flight data acquired at 0.14 mm isotropic resolution from Figure 7 was manually segmented. In this example, it is clear that the automatic segmentation is missing several small vessel branches that could be readily segmented manually. The maximum intensity projection contains 50 slices, corresponding to 7-mm coverage in the head-foot direction. Improved performance of this manual segmentation generated on a per slice basis using the full 3D information shows the potential for advances in automatic segmentation algorithms to identify many more pial arteries in this data than which are visible in the maximum intensity projections presented here.

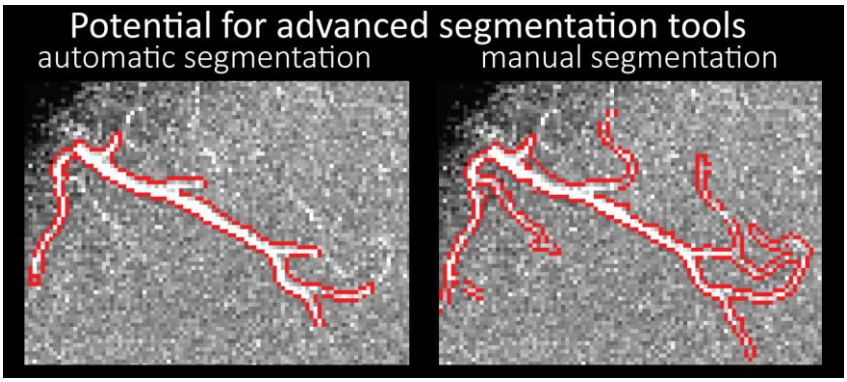

Supplementary Figure 11: Small section of the time-of-flight data (13.44 mm × 9.94 mm × 7 mm) acquired at 0.14 mm isotropic resolution and the corresponding segmentation of the pial arterial vasculature from Figure 7 showing the performance of the automatic segmentation used in this study (LEFT) and manual segmentation (RIGHT).

Acknowledgements

We thank Mr. Kyle Droppa and Ms. Nina Fultz for help with subject recruitment and MRI scanner operation. This work was supported in part by the NIH NIBIB (grants P41-EB015896, P41-EB030006 and R01-EB019437), NINDS (grant R21-NS106706), the *BRAIN Initiative* (NIH NIMH grants R01-MH111438 and R01-MH111419), the Natural Sciences and Engineering Research Council of Canada (NSERC), the *Fonds de recherche Nature et technologies* (FQRNT), the German Research Foundation (DFG) (MA 9235/1-1), and the MGH/HST Athinoula A. Martinos Center for Biomedical Imaging; and was made possible by the resources provided by NIH Shared Instrumentation Grants S10-RR019371 and S10-OD02363701. SRR was supported by the Marie Skłodowska-Curie Action MS-fMRI-QSM 794298.

References

Al-Kwifi, O., Emery, D.J., Wilman, A.H., 2002. Vessel contrast at three Tesla in time-of-flight magnetic resonance angiography of the intracranial and carotid arteries. Magn. Reson. Imaging 20, 181–187. https://doi.org/10.1016/S0730-725X(02)00486-1

Alpers, B.J., Berry, R.G., Paddison, R.M., 1959. Anatomical Studies of the Circle of Willis in Normal Brain. AMA Arch. Neurol. Psychiatry 81, 409–418. https://doi.org/10.1001/archneurpsyc.1959.02340160007002

Alsop, D.C., Detre, J.A., Golay, X., Günther, M., Hendrikse, J., Hernandez-Garcia, L., Lu, H., MacIntosh, B.J., Parkes, L.M., Smits, M., van Osch, M.J.P., Wang, D.J.J., Wong, E.C., Zaharchuk, G., 2015. Recommended implementation of arterial spin-labeled perfusion MRI for clinical applications: A consensus of the ISMRM perfusion study group and the European consortium for ASL in dementia. Magn. Reson. Med. 73, 102–116. https://doi.org/10.1002/mrm.25197

Amemiya, S., Takao, H., Abe, O., 2020. Origin of the Time Lag Phenomenon and the Global Signal in Resting-State fMRI. Front. Neurosci. 14. https://doi.org/10.3389/fnins.2020.596084

Andersson, J.L.R., Skare, S., Ashburner, J., 2003. How to correct susceptibility distortions in spin-echo echo-planar images: application to diffusion tensor imaging. NeuroImage 20, 870–888. https://doi.org/10.1016/S1053-8119(03)00336-7

Arts, T., Meijs, T.A., Grotenhuis, H., Voskuil, M., Siero, J., Biessels, G.J., Zwanenburg, J., 2021. Velocity and Pulsatility Measures in the Perforating Arteries of the Basal Ganglia at 3T MRI in Reference to 7T MRI. Front. Neurosci. 15.

Atkinson, D., Brant-Zawadzki, M., Gillan, G., Purdy, D., Laub, G., 1994. Improved MR angiography: magnetization transfer suppression with variable flip angle excitation and increased resolution. Radiology 190, 890–894. https://doi.org/10.1148/radiology.190.3.8115646

Avants, B.B., Tustison, N., Song, G., 2009. Advanced normalization tools (ANTS). Insight J 2, 1–35.

Bae, K.T., Park, S.-H., Moon, C.-H., Kim, J.-H., Kaya, D., Zhao, T., 2010. Dual-echo arteriovenography imaging with 7T MRI: CODEA with 7T. J. Magn. Reson. Imaging 31, 255–261. https://doi.org/10.1002/jmri.22019

Baran, U., Wang, R.K., 2016. Review of optical coherence tomography based angiography in neuroscience. Neurophotonics 3, 010902. https://doi.org/10.1117/1.NPh.3.1.010902

Bartholdi, E., Ernst, R.R., 1973. Fourier spectroscopy and the causality principle. J. Magn. Reson. 1969 11, 9–19. https://doi.org/10.1016/0022-2364(73)90076-0

Baumbach, G.L., Heistad, D.D., 1985. Regional, segmental, and temporal heterogeneity of cerebral vascular autoregulation. Ann. Biomed. Eng. 13, 303–310. https://doi.org/10.1007/BF02584248

Beevor, C.E., Ferrier, D., 1909. I. On the distribution of the different arteries supplying the human brain. Philos. Trans. R. Soc. Lond. Ser. B Contain. Pap. Biol. Character 200, 1–55. https://doi.org/10.1098/rstb.1909.0001

Bernier, M., Cunnane, S.C., Whittingstall, K., 2018. The morphology of the human cerebrovascular system. Hum. Brain Mapp. 39, 4962–4975. https://doi.org/10.1002/hbm.24337

Bizeau, A., Gilbert, G., Bernier, M., Huynh, M.T., Bocti, C., Descoteaux, M., Whittingstall, K., 2018. Stimulus-evoked changes in cerebral vessel diameter: A study in healthy humans. J. Cereb. Blood Flow Metab. 38, 528–539. https://doi.org/10.1177/0271678X17701948

Blinder, P., Shih, A.Y., Rafie, C., Kleinfeld, D., 2010. Topological basis for the robust distribution of blood to rodent neocortex. Proc. Natl. Acad. Sci. 107, 12670–12675. https://doi.org/10.1073/pnas.1007239107

Bouvy, W.H., Biessels, G.J., Kuijf, H.J., Kappelle, L.J., Luijten, P.R., Zwanenburg, J.J.M., 2014. Visualization of Perivascular Spaces and Perforating Arteries With 7 T Magnetic Resonance Imaging: Invest. Radiol. 49, 307–313. https://doi.org/10.1097/RLI.0000000000000027

Bouvy, W.H., Geurts, L.J., Kuijf, H.J., Luijten, P.R., Kappelle, L.J., Biessels, G.J., Zwanenburg, J.J.M., 2016. Assessment of blood flow velocity and pulsatility in cerebral perforating arteries with 7-T

quantitative flow MRI: Blood Flow Velocity And Pulsatility In Cerebral Perforating Arteries. NMR Biomed. 29, 1295–1304. https://doi.org/10.1002/nbm.3306

Bright, M.G., Whittaker, J.R., Driver, I.D., Murphy, K., 2020. Vascular physiology drives functional brain networks. NeuroImage 217, 116907. https://doi.org/10.1016/j.neuroimage.2020.116907

Brown, R.W., Cheng, Y.-C.N., Haacke, E.M., Thompson, M.R., Venkatesan, R., 2014a. Chapter 24 - MR Angiography and Flow Quantification, in: Magnetic Resonance Imaging. John Wiley & Sons, Ltd, pp. 701–737. https://doi.org/10.1002/9781118633953.ch24

Brown, R.W., Cheng, Y.-C.N., Haacke, E.M., Thompson, M.R., Venkatesan, R., 2014b. Chapter 23 - Motion Artifacts and Flow Compensation, in: Magnetic Resonance Imaging. John Wiley & Sons, Inc., Hoboken, NJ, USA, pp. 669–700. https://doi.org/10.1002/9781118633953.ch23

Brown, R.W., Cheng, Y.-C.N., Haacke, E.M., Thompson, M.R., Venkatesan, R., 2014c. Chapter 15 - Signal, Contrast, and Noise, in: Magnetic Resonance Imaging. John Wiley & Sons, Ltd, pp. 325–373. https://doi.org/10.1002/9781118633953.ch15

Bui, A.V., Manasseh, R., Liffman, K., Šutalo, I.D., 2010. Development of optimized vascular fractal tree models using level set distance function. Med. Eng. Phys. 32, 790–794. https://doi.org/10.1016/j.medengphy.2010.04.014

Callaghan, M.F., Josephs, O., Herbst, M., Zaitsev, M., Todd, N., Weiskopf, N., 2015. An evaluation of prospective motion correction (PMC) for high resolution quantitative MRI. Front. Neurosci. 9. https://doi.org/10.3389/fnins.2015.00097

Candes, E.J., Romberg, J., Tao, T., 2006. Robust uncertainty principles: exact signal reconstruction from highly incomplete frequency information. IEEE Trans. Inf. Theory 52, 489–509. https://doi.org/10.1109/TIT.2005.862083

Carr, J.C., Carroll, T.J., 2012. Magnetic resonance angiography: principles and applications. Springer, New York.

Cassot, F., Lauwers, F., Fouard, C., Prohaska, S., Lauwers-Cances, V., 2006. A Novel Three-Dimensional Computer-Assisted Method for a Quantitative Study of Microvascular Networks of the Human Cerebral Cortex. Microcirculation 13, 1–18. https://doi.org/10.1080/10739680500383407

Chen, J.E., Lewis, L.D., Chang, C., Tian, Q., Fultz, N.E., Ohringer, N.A., Rosen, B.R., Polimeni, J.R., 2020. Resting-state "physiological networks." NeuroImage 213, 116707. https://doi.org/10.1016/j.neuroimage.2020.116707

Chen, L., Mossa-Basha, M., Balu, N., Canton, G., Sun, J., Pimentel, K., Hatsukami, T.S., Hwang, J.-N., Yuan, C., 2018. Development of a quantitative intracranial vascular features extraction tool on 3DMRA using semiautomated open-curve active contour vessel tracing: Comprehensive Artery Features Extraction From 3D MRA. Magn. Reson. Med. 79, 3229–3238. https://doi.org/10.1002/mrm.26961

Cho, Z.-H., Kang, C.-K., Han, J.-Y., Kim, S.-H., Park, C.-A., Kim, K.-N., Hong, S.-M., Park, C.-W., Kim, Y.-B., 2008. Functional MR angiography with 7.0 T. NeuroImage 42, 70–75. https://doi.org/10.1016/j.neuroimage.2008.05.003

Cho, Z.-H., Kang, C.-K., Park, C.-A., Hong, S.-M., Kim, S.-H., Oh, S.-T., Kim, Y.-B., 2012. Microvascular functional MR angiography with ultra-high-field 7 t MRI: Comparison with BOLD fMRI. Int. J. Imaging Syst. Technol. 22, 18–22. https://doi.org/10.1002/ima.22008

Choi, U.-S., Kawaguchi, H., Kida, I., 2020. Cerebral artery segmentation based on magnetization-prepared two rapid acquisition gradient echo multi-contrast images in 7 Tesla magnetic resonance imaging. NeuroImage 222, 117259. https://doi.org/10.1016/j.neuroimage.2020.117259

Cilliers, K., Page, B.J., 2017. Description of the anterior cerebral artery and its cortical branches: Variation in presence, origin, and size. Clin. Neurol. Neurosurg. 152, 78–83. https://doi.org/10.1016/j.clineuro.2016.11.024

Cipolla, M.J., 2009. Chapter 2: Anatomy and Ultrastructure, in: The Cerebral Circulation. Morgan & Claypool Life Sciences.

Conolly, S., Nishimura, D., Macovski, A., Glover, G., 1988. Variable-rate selective excitation. J. Magn. Reson. 1969 78, 440–458. https://doi.org/10.1016/0022-2364(88)90131-X

Constantinides, C.D., Atalar, E., McVeigh, E.R., 1997. Signal-to-noise measurements in magnitude images from NMR phased arrays. Magn. Reson. Med. 38, 852–857. https://doi.org/10.1002/mrm.1910380524

Deistung, A., Dittrich, E., Sedlacik, J., Rauscher, A., Reichenbach, J.R., 2009. ToF-SWI: Simultaneous time of flight and fully flow compensated susceptibility weighted imaging. J. Magn. Reson. Imaging 29, 1478–1484. https://doi.org/10.1002/jmri.21673

Detre, J.A., Leigh, J.S., Williams, D.S., Koretsky, A.P., 1992. Perfusion imaging. Magn. Reson. Med. 23, 37–45. https://doi.org/10.1002/mrm.1910230106

Djulejić, V., Marinković, S., Milić, V., Georgievski, B., Rašić, M., Aksić, M., Puškaš, L., 2015. Common features of the cerebral perforating arteries and their clinical significance. Acta Neurochir. (Wien) 157, 743–754. https://doi.org/10.1007/s00701-015-2378-8

Drew, P.J., Mateo, C., Turner, K.L., Yu, X., Kleinfeld, D., 2020. Ultra-slow Oscillations in fMRI and Resting-State Connectivity: Neuronal and Vascular Contributions and Technical Confounds. Neuron 107, 782–804. https://doi.org/10.1016/j.neuron.2020.07.020

Du, Y., Parker, D.L., Davis, W.L., Blatter, D.D., 1993. Contrast-to-Noise-Ratio Measurements in Three-Dimensional Magnetic Resonance Angiography. Invest. Radiol. 28, 1004–1009.

Du, Y.P., Jin, Z., 2008. Simultaneous acquisition of MR angiography and venography (MRAV). Magn. Reson. Med. 59, 954–958. https://doi.org/10.1002/mrm.21581

Du, Y.P., Parker, D.L., Davis, W.L., Cao, G., 1994. Reduction of partial-volume artifacts with zero-filled interpolation in three-dimensional MR angiography. J. Magn. Reson. Imaging 4, 733–741. https://doi.org/10.1002/jmri.1880040517

Du, Y.P., Parker, D.L., Davis, W.L., Cao, G., Buswell, H.R., Goodrich, K.C., 1996. Experimental and theoretical studies of vessel contrast-to-noise ratio in intracranial time-of-flight MR angiography. J. Magn. Reson. Imaging 6, 99–108. https://doi.org/10.1002/jmri.1880060120

Duvernoy, H., Delon, S., Vannson, J.L., 1983. The Vascularization of The Human Cerebellar Cortex. Brain Res. Bull. 11, 419–480.

Duvernoy, H.M., 1999. The Human Brain: Surface, Blood Supply, and Three-Dimensional Sectional Anatomy. Springer, Vienna, S.l.

Duvernoy, H.M., Delon, S., Vannson, J.L., 1981. Cortical blood vessels of the human brain. Brain Res. Bull. 7, 519–579. https://doi.org/10.1016/0361-9230(81)90007-1

Eckstein, K., Bachrata, B., Hangel, G., Widhalm, G., Enzinger, C., Barth, M., Trattnig, S., Robinson, S.D., 2021. Improved susceptibility weighted imaging at ultra-high field using bipolar multi-echo acquisition and optimized image processing: CLEAR-SWI. NeuroImage 237, 118175. https://doi.org/10.1016/j.neuroimage.2021.118175

Edelstein, W.A., Glover, G.H., Hardy, C.J., Redington, R.W., 1986. The intrinsic signal-to-noise ratio in NMR imaging. Magn. Reson. Med. 3, 604–618. https://doi.org/10.1002/mrm.1910030413

Ernst, R.R., Anderson, W.A., 1966. Application of Fourier Transform Spectroscopy to Magnetic Resonance. Rev. Sci. Instrum. 37, 93–102. https://doi.org/10.1063/1.1719961

Fan, A.P., Govindarajan, S.T., Kinkel, R.P., Madigan, N.K., Nielsen, A.S., Benner, T., Tinelli, E., Rosen, B.R., Adalsteinsson, E., Mainero, C., 2015. Quantitative oxygen extraction fraction from 7-Tesla MRI phase: reproducibility and application in multiple sclerosis. J. Cereb. Blood Flow Metab. Off. J. Int. Soc. Cereb. Blood Flow Metab. 35, 131–139. https://doi.org/10.1038/jcbfm.2014.187

Fiedler, T.M., Ladd, M.E., Bitz, A.K., 2018. SAR Simulations & Safety. NeuroImage 168, 33–58. https://doi.org/10.1016/j.neuroimage.2017.03.035

Frangi, A.F., Niessen, W.J., Vincken, K.L., Viergever, M.A., 1998. Multiscale vessel enhancement filtering, in: Wells, W.M., Colchester, A., Delp, S. (Eds.), Medical Image Computing and Computer-Assisted Intervention — MICCAI'98, Lecture Notes in Computer Science. Springer, Berlin, Heidelberg, pp. 130–137. https://doi.org/10.1007/BFb0056195

Frässle, S., Aponte, E.A., Bollmann, S., Brodersen, K.H., Do, C.T., Harrison, O.K., Harrison, S.J., Heinzle, J., Iglesias, S., Kasper, L., Lomakina, E.I., Mathys, C., Müller-Schrader, M., Pereira, I., Petzschner, F.H., Raman, S., Schöbi, D., Toussaint, B., Weber, L.A., Yao, Y., Stephan, K.E., 2021. TAPAS: An Open-Source Software Package for Translational Neuromodeling and Computational Psychiatry. Front. Psychiatry 12. https://doi.org/10.3389/fpsyt.2021.680811

Ginat, D.T., Smith, E.R., Robertson, R.L., Scott, R.M., Schaefer, P.W., 2013. Imaging After Direct and Indirect Extracranial-Intracranial Bypass Surgery. Am. J. Roentgenol. 201, W124–W132. https://doi.org/10.2214/AJR.12.9517

Ginsberg, M.D., 2018. The cerebral collateral circulation: Relevance to pathophysiology and treatment of stroke. Neuropharmacology, Cerebral Ischemia 134, 280–292. https://doi.org/10.1016/j.neuropharm.2017.08.003

Gomes, F.B., Dujovny, M., Umansky, F., Berman, S.K., Diaz, F.G., Ausman, J.I., Mirchandani, H.G., Ray, W.J., 1986. Microanatomy of the anterior cerebral artery. Surg. Neurol. 26, 129–141. https://doi.org/10.1016/0090-3019(86)90365-4

Griswold, M.A., Jakob, P.M., Heidemann, R.M., Nittka, M., Jellus, V., Wang, J., Kiefer, B., Haase, A., 2002. Generalized autocalibrating partially parallel acquisitions (GRAPPA). Magn. Reson. Med. 47, 1202–1210. https://doi.org/10.1002/mrm.10171

Gulban, O.F., Bollmann, S., Huber, R., Wagstyl, K., Goebel, R., Poser, B.A., Kay, K., Ivanov, D., 2021. Mesoscopic Quantification of Cortical Architecture in the Living Human Brain. https://doi.org/10.1101/2021.11.25.470023

Haacke, E.M., Masaryk, T.J., Wielopolski, P.A., Zypman, F.R., Tkach, J.A., Amartur, S., Mitchell, J., Clampitt, M., Paschal, C., 1990. Optimizing blood vessel contrast in fast three-dimensional MRI. Magn. Reson. Med. 14, 202–221. https://doi.org/10.1002/mrm.1910140207

Havlicek, M., Uludağ, K., 2020. A dynamical model of the laminar BOLD response. NeuroImage 204, 116209. https://doi.org/10.1016/j.neuroimage.2019.116209

Helthuis, J.H.G., van Doormaal, T.P.C., Hillen, B., Bleys, R.L.A.W., Harteveld, A.A., Hendrikse, J., van der Toorn, A., Brozici, M., Zwanenburg, J.J.M., van der Zwan, A., 2019. Branching Pattern of the Cerebral Arterial Tree. Anat. Rec. 302, 1434–1446. https://doi.org/10.1002/ar.23994

Herz, D.A., Baez, S., Shulman, K., 1975. Pial Microcirculation in Subarachnoid Hemorrhage. Stroke 6, 417–424. https://doi.org/10.1161/01.STR.6.4.417

Hetts, S.W., Yen, A., Cooke, D.L., Nelson, J., Jolivalt, P., Banaga, J., Amans, M.R., Dowd, C.F., Higashida, R.T., Lawton, M.T., Kim, H., Halbach, V.V., 2017. Pial Artery Supply as an Anatomic Risk Factor for Ischemic Stroke in the Treatment of Intracranial Dural Arteriovenous Fistulas. Am. J. Neuroradiol. 38, 2315–2320. https://doi.org/10.3174/ajnr.A5396

Heverhagen, J.T., Bourekas, E., Sammet, S., Knopp, M.V., Schmalbrock, P., 2008. Time-of-Flight Magnetic Resonance Angiography at 7 Tesla. Invest. Radiol. 43, 568–573. https://doi.org/10.1097/RLI.0b013e31817e9b2c

Hilbert, A., Madai, V.I., Akay, E.M., Aydin, O.U., Behland, J., Sobesky, J., Galinovic, I., Khalil, A.A., Taha, A.A., Wuerfel, J., Dusek, P., Niendorf, T., Fiebach, J.B., Frey, D., Livne, M., 2020. BRAVE-NET: Fully Automated Arterial Brain Vessel Segmentation in Patients With Cerebrovascular Disease. Front. Artif. Intell. 3. https://doi.org/10.3389/frai.2020.552258

Hillman, E.M.C., Devor, A., Bouchard, M.B., Dunn, A.K., Krauss, G.W., Skoch, J., Bacskai, B.J., Dale, A.M., Boas, D.A., 2007. Depth-resolved optical imaging and microscopy of vascular compartment dynamics during somatosensory stimulation. NeuroImage 35, 89–104. https://doi.org/10.1016/j.neuroimage.2006.11.032

Hirsch, S., Reichold, J., Schneider, M., Székely, G., Weber, B., 2012. Topology and Hemodynamics of the Cortical Cerebrovascular System. J. Cereb. Blood Flow Metab. 32, 952–967. https://doi.org/10.1038/jcbfm.2012.39

Hofman, M.B.M., Visser, F.C., Rossum, A.C.V., Vink, G.Q.M., Sprenger, M., Westerhof, N., 1995. In Vivo Validation of Magnetic Resonance Blood Volume Flow Measurements with Limited Spatial

Resolution in Small Vessels. Magn. Reson. Med. 33, 778–784. https://doi.org/10.1002/mrm.1910330606
Hoogeveen, R.M., Bakker, C.J.G., Viergever, M.A., 1998. Limits to the accuracy of vessel diameter measurement in MR angiography. J. Magn. Reson. Imaging 8, 1228–1235. https://doi.org/10.1002/jmri.1880080608
Hsu, C., Li, Y., Han, Y., Elijovich, L., Sabin, N.D., Abuelem, T., Torabi, R., Faught, A., Hua, C., Klimo, P., Merchant, T.E., Lucas, J.T., 2019. Automatic image processing pipeline for tracking longitudinal vessel changes in magnetic resonance angiography. J. Magn. Reson. Imaging 50, 1063–1074. https://doi.org/10.1002/jmri.26699
Hsu, C.-Y., Ghaffari, M., Alaraj, A., Flannery, M., Zhou, X.J., Linninger, A., 2017. Gap-free segmentation of vascular networks with automatic image processing pipeline. Comput. Biol. Med. 82, 29–39. https://doi.org/10.1016/j.compbiomed.2017.01.012
Hua, J., Liu, P., Kim, T., Donahue, M., Rane, S., Chen, J.J., Qin, Q., Kim, S.-G., 2019. MRI techniques to measure arterial and venous cerebral blood volume. NeuroImage 187, 17–31. https://doi.org/10.1016/j.neuroimage.2018.02.027
Huber, L., 2014. Mapping Human Brain Activity by Functional Magnetic Resonance Imaging of Blood Volume. Fakultät für Physik und Geowissenschaften der Universität Leipzig.
Huber, L., Ivanov, D., Krieger, S.N., Streicher, M.N., Mildner, T., Poser, B.A., Möller, H.E., Turner, R., 2014. Slab-selective, BOLD-corrected VASO at 7 Tesla provides measures of cerebral blood volume reactivity with high signal-to-noise ratio: SS-SI-VASO Measures Changes of CBV in Brain. Magn. Reson. Med. 72, 137–148. https://doi.org/10.1002/mrm.24916
Huck, J., Wanner, Y., Fan, A.P., Jäger, A.-T., Grahl, S., Schneider, U., Villringer, A., Steele, C.J., Tardif, C.L., Bazin, P.-L., Gauthier, C.J., 2019. High resolution atlas of the venous brain vasculature from 7 T quantitative susceptibility maps. Brain Struct. Funct. 224, 2467–2485. https://doi.org/10.1007/s00429-019-01919-4
Ii, S., Kitade, H., Ishida, S., Imai, Y., Watanabe, Y., Wada, S., 2020. Multiscale modeling of human cerebrovasculature: A hybrid approach using image-based geometry and a mathematical algorithm. PLOS Comput. Biol. 16, e1007943. https://doi.org/10.1371/journal.pcbi.1007943
Iliff, J.J., Wang, M., Zeppenfeld, D.M., Venkataraman, A., Plog, B.A., Liao, Y., Deane, R., Nedergaard, M., 2013. Cerebral Arterial Pulsation Drives Paravascular CSF–Interstitial Fluid Exchange in the Murine Brain. J. Neurosci. 33, 18190–18199. https://doi.org/10.1523/JNEUROSCI.1592-13.2013
Jezzard, P., Clare, S., 1999. Sources of distortion in functional MRI data. Hum. Brain Mapp. 8, 80–85. https://doi.org/10.1002/(SICI)1097-0193(1999)8:2/3<80::AID-HBM2>3.0.CO;2-C
Johst, S., Wrede, K.H., Ladd, M.E., Maderwald, S., 2012. Time-of-Flight Magnetic Resonance Angiography at 7 T Using Venous Saturation Pulses With Reduced Flip Angles. Invest. Radiol. 47, 445–450. https://doi.org/10.1097/RLI.0b013e31824ef21f
Jones, E.G., 1970. On the mode of entry of blood vessels into the cerebral cortex. J. Anat. 106, 507–520.
Kang, C.-K., Park, C.-A., Kim, K.-N., Hong, S.-M., Park, C.-W., Kim, Y.-B., Cho, Z.-H., 2010. Non-invasive visualization of basilar artery perforators with 7T MR angiography. J. Magn. Reson. Imaging 32, 544–550. https://doi.org/10.1002/jmri.22250
Kasper, L., Engel, M., Barmet, C., Haeberlin, M., Wilm, B.J., Dietrich, B.E., Schmid, T., Gross, S., Brunner, D.O., Stephan, K.E., Pruessmann, K.P., 2018. Rapid anatomical brain imaging using spiral acquisition and an expanded signal model. NeuroImage 168, 88–100. https://doi.org/10.1016/j.neuroimage.2017.07.062
Keelan, J., Chung, E.M.L., Hague, J.P., 2019. Development of a globally optimised model of the cerebral arteries. Phys. Med. Biol. 64, 125021. https://doi.org/10.1088/1361-6560/ab2479
Kiselev, V.G., Strecker, R., Ziyeh, S., Speck, O., Hennig, J., 2005. Vessel size imaging in humans. Magn. Reson. Med. 53, 553–563. https://doi.org/10.1002/mrm.20383

Klepaczko, A., Szczypiński, P., Deistung, A., Reichenbach, J.R., Materka, A., 2016. Simulation of MR angiography imaging for validation of cerebral arteries segmentation algorithms. Comput. Methods Programs Biomed. 137, 293–309. https://doi.org/10.1016/j.cmpb.2016.09.020

Kobari, M., Gotoh, F., Fukuuchi, Y., Tanaka, K., Suzuki, N., Uematsu, D., 1984. Blood Flow Velocity in the Pial Arteries of Cats, with Particular Reference to the Vessel Diameter. J. Cereb. Blood Flow Metab. 4, 110–114. https://doi.org/10.1038/jcbfm.1984.15

Korin, H.W., Riederer, S.J., Bampton, A.E.H., Ehman, R.L., 1992. Altered phase-encoding order for reduced sensitivity to motion in three-dimensional MR imaging. J. Magn. Reson. Imaging 2, 687–693. https://doi.org/10.1002/jmri.1880020613

Ladd, M.E., 2007. High-Field-Strength Magnetic Resonance: Potential and Limits. Top Magn Reson Imaging 18, 139–152.

LeCun, Y., Bengio, Y., Hinton, G., 2015. Deep learning. Nature 521, 436–444. https://doi.org/10.1038/nature14539

Lee, H.-W., Caldwell, J.E., Dodson, B., Talke, P., Howley, J., 1997. The Effect of Clonidine on Cerebral Blood Flow Velocity, Carbon Dioxide Cerebral Vasoreactivity, and Response to Increased Arterial Pressure in Human Volunteers. Anesthesiol. J. Am. Soc. Anesthesiol. 87, 553–558.

Lesage, D., Angelini, E.D., Bloch, I., Funka-Lea, G., 2009. A review of 3D vessel lumen segmentation techniques: Models, features and extraction schemes. Med. Image Anal. 13, 819–845. https://doi.org/10.1016/j.media.2009.07.011

Lüsebrink, F., Mattern, H., Yakupov, R., Acosta-Cabronero, J., Ashtarayeh, M., Oeltze-Jafra, S., Speck, O., 2021. Comprehensive ultrahigh resolution whole brain in vivo MRI dataset as a human phantom. Sci. Data 8, 138. https://doi.org/10.1038/s41597-021-00923-w

Lüsebrink, F., Sciarra, A., Mattern, H., Yakupov, R., Speck, O., 2017. T 1 -weighted in vivo human whole brain MRI dataset with an ultrahigh isotropic resolution of 250 µm. Sci. Data 4, 170032. https://doi.org/10.1038/sdata.2017.32

Maderwald, S., Ladd, S.C., Gizewski, E.R., Kraff, O., Theysohn, J.M., Wicklow, K., Moenninghoff, C., Wanke, I., Ladd, M.E., Quick, H.H., 2008. To TOF or not to TOF: strategies for non-contrast-enhanced intracranial MRA at 7 T. Magn. Reson. Mater. Phys. Biol. Med. 21, 159. https://doi.org/10.1007/s10334-007-0096-9

Manjón, J.V., Coupé, P., Martí-Bonmatí, L., Collins, D.L., Robles, M., 2010. Adaptive non-local means denoising of MR images with spatially varying noise levels. J. Magn. Reson. Imaging 31, 192–203. https://doi.org/10.1002/jmri.22003

Mansfield, P., Harvey, P.R., 1993. Limits to neural stimulation in echo-planar imaging. Magn. Reson. Med. 29, 746–758. https://doi.org/10.1002/mrm.1910290606

Marín-Padilla, M., 2012. The human brain intracerebral microvascular system: development and structure. Front. Neuroanat. 6. https://doi.org/10.3389/fnana.2012.00038

Markuerkiaga, I., Barth, M., Norris, D.G., 2016. A cortical vascular model for examining the specificity of the laminar BOLD signal. Neuroimage 132, 491–8. https://doi.org/10.1016/j.neuroimage.2016.02.073

Masaryk, T.J., Modic, M.T., Ross, J.S., Ruggieri, P.M., Laub, G.A., Lenz, G.W., Haacke, E.M., Selman, W.R., Wiznitzer, M., Harik, S.I., 1989. Intracranial circulation: preliminary clinical results with three-dimensional (volume) MR angiography. Radiology 171, 793–799. https://doi.org/10.1148/radiology.171.3.2717754

Mastorakos, P., McGavern, D., 2019. The anatomy and immunology of vasculature in the central nervous system. Sci. Immunol. 4. https://doi.org/10.1126/sciimmunol.aav0492

Mattern, H., Sciarra, A., Godenschweger, F., Stucht, D., Lüsebrink, F., Rose, G., Speck, O., 2018. Prospective motion correction enables highest resolution time-of-flight angiography at 7T: Prospectively Motion-Corrected TOF Angiography at 7T. Magn. Reson. Med. 80, 248–258. https://doi.org/10.1002/mrm.27033

Mattern, H., Sciarra, A., Lüsebrink, F., Acosta-Cabronero, J., Speck, O., 2019. Prospective motion correction improves high-resolution quantitative susceptibility mapping at 7T. Magn. Reson. Med. 81, 1605–1619. https://doi.org/10.1002/mrm.27509

McConnell, E.D., Wei, H.S., Reitz, K.M., Kang, H., Takano, T., Vates, G.E., Nedergaard, M., 2016. Cerebral microcirculatory failure after subarachnoid hemorrhage is reversed by hyaluronidase. J. Cereb. Blood Flow Metab. 36, 1537–1552. https://doi.org/10.1177/0271678X15608389

Mchedlishvili, G., Kuridze, N., 1984. The Modular Organization of the Pial Arterial System in Phylogeny. J. Cereb. Blood Flow Metab. 4, 391–396. https://doi.org/10.1038/jcbfm.1984.57

Meixner, C.R., Liebig, P., Speier, P., Forman, C., Hensel, B., Schmidt, M., Saake, M., Uder, M., Doerfler, A., Heidemann, R.M., Schmitter, S., Nagel, A.M., 2019. High resolution time-of-flight MR-angiography at 7 T exploiting VERSE saturation, compressed sensing and segmentation. Magn. Reson. Imaging 63, 193–204. https://doi.org/10.1016/j.mri.2019.08.014

Moccia, S., De Momi, E., El Hadji, S., Mattos, L.S., 2018. Blood vessel segmentation algorithms — Review of methods, datasets and evaluation metrics. Comput. Methods Programs Biomed. 158, 71–91. https://doi.org/10.1016/j.cmpb.2018.02.001

Molinari, F., Liboni, W., Grippi, G., Negri, E., 2006. Relationship between oxygen supply and cerebral blood flow assessed by transcranial Doppler and near-infrared spectroscopy in healthy subjects during breath-holding. J. Neuroengineering Rehabil. 3, 16–16. https://doi.org/10.1186/1743-0003-3-16

Mut, F., Wright, S., Ascoli, G.A., Cebral, J.R., 2014. Morphometric, geographic, and territorial characterization of brain arterial trees. Int. J. Numer. Methods Biomed. Eng. 30, 755–766. https://doi.org/10.1002/cnm.2627

Nagaoka, T., Yoshida, A., 2006. Noninvasive Evaluation of Wall Shear Stress on Retinal Microcirculation in Humans. Investig. Opthalmology Vis. Sci. 47, 1113. https://doi.org/10.1167/iovs.05-0218

Nägele, T., Klose, U., Grodd, W., Voigt, K., Nüsslin, F., 1995. Nonlinear excitation profiles for three-dimensional inflow MR angiography. J. Magn. Reson. Imaging 5, 416–420. https://doi.org/10.1002/jmri.1880050408

Nishimura, D.G., Irarrazabal, P., Meyer, C.H., 1995. A Velocity k-Space Analysis of Flow Effects in Echo-Planar and Spiral Imaging. Magn. Reson. Med. 33, 549–556. https://doi.org/10.1002/mrm.1910330414

Nishimura, D.G., Jackson, J.I., Pauly, J.M., 1991. On the nature and reduction of the displacement artifact in flow images. Magn. Reson. Med. 22, 481–492. https://doi.org/10.1002/mrm.1910220255

Nonaka, H., Akima, M., Hatori, T., Nagayama, T., Zhang, Z., Ihara, F., 2003a. Microvasculature of the human cerebral white matter: Arteries of the deep white matter. Neuropathology 23, 111–118. https://doi.org/10.1046/j.1440-1789.2003.00486.x

Nonaka, H., Akima, M., Nagayama, T., Hatori, T., Zhang, Z., Ihara, F., 2003b. Microvasculature of the human cerebral meninges. Neuropathology 23, 129–135. https://doi.org/10.1046/j.1440-1789.2003.00487.x

North, D.O., 1963. An Analysis of the factors which determine signal/noise discrimination in pulsed-carrier systems. Proc. IEEE 51, 1016–1027. https://doi.org/10.1109/PROC.1963.2383

Nowinski, W.L., Chua, B.C., Marchenko, Y., Puspitsari, F., Volkau, I., Knopp, M.V., 2011. Three-dimensional reference and stereotactic atlas of human cerebrovasculature from 7Tesla. NeuroImage 55, 986–998. https://doi.org/10.1016/j.neuroimage.2010.12.079

Ogawa, S., Lee, T.M., Kay, A.R., Tank, D.W., 1990. Brain magnetic resonance imaging with contrast dependent on blood oxygenation. Proc. Natl. Acad. Sci. 87, 9868–9872. https://doi.org/10.1073/pnas.87.24.9868

Papantchev, V., Stoinova, V., Aleksandrov, A., Todorova-Papantcheva, D., Hristov, S., Petkov, D., Nachev, G., Ovtscharoff, W., 2013. The role of Willis circle variations during unilateral selective

cerebral perfusion: a study of 500 circles. Eur. J. Cardiothorac. Surg. 44, 743–753. https://doi.org/10.1093/ejcts/ezt103

Park, C.S., Hartung, G., Alaraj, A., Du, X., Charbel, F.T., Linninger, A.A., 2020. Quantification of blood flow patterns in the cerebral arterial circulation of individual (human) subjects. Int. J. Numer. Methods Biomed. Eng. 36. https://doi.org/10.1002/cnm.3288

Parker, D.L., Goodrich, K.C., Roberts, J.A., Chapman, B.E., Jeong, E.-K., Kim, S.-E., Tsuruda, J.S., Katzman, G.L., 2003. The need for phase-encoding flow compensation in high-resolution intracranial magnetic resonance angiography. J. Magn. Reson. Imaging 18, 121–127. https://doi.org/10.1002/jmri.10322

Parker, D.L., Yuan, C., Blatter, D.D., 1991. MR angiography by multiple thin slab 3D acquisition. Magn. Reson. Med. 17, 434–451. https://doi.org/10.1002/mrm.1910170215

Pauling, L., Coryell, C.D., 1936. The magnetic properties and structure of hemoglobin, oxyhemoglobin and carbonmonoxyhemoglobin. Proc. Natl. Acad. Sci. 22, 210–216. https://doi.org/10.1073/pnas.22.4.210

Payne, S.J., 2017. Cerebral Blood Flow And Metabolism: A Quantitative Approach. World Scientific.

Peters, A.M., Brookes, M.J., Hoogenraad, F.G., Gowland, P.A., Francis, S.T., Morris, P.G., Bowtell, R., 2007. T2* measurements in human brain at 1.5, 3 and 7 T. Magn. Reson. Imaging 25, 748–753. https://doi.org/10.1016/j.mri.2007.02.014

Phellan, R., Forkert, N.D., 2017. Comparison of vessel enhancement algorithms applied to time-of-flight MRA images for cerebrovascular segmentation. Med. Phys. 44, 5901–5915. https://doi.org/10.1002/mp.12560

Pipe, J.G., 2001. Limits of Time-of-Flight Magnetic Resonance Angiography. Top. Magn. Reson. Imaging 12, 163–174.

Pohmann, R., Speck, O., Scheffler, K., 2016. Signal-to-Noise Ratio and MR Tissue Parameters in Human Brain Imaging at 3, 7, and 9.4 Tesla Using Current Receive Coil Arrays. Magn. Reson. Med. 75, 801–809. https://doi.org/10.1002/mrm.25677

Polimeni, J.R., Fischl, B., Greve, D.N., Wald, L.L., 2010. Laminar analysis of 7T BOLD using an imposed spatial activation pattern in human V1. Neuroimage 52, 1334–46. https://doi.org/10.1016/j.neuroimage.2010.05.005

Pruessmann, K.P., Weiger, M., Scheidegger, M.B., Boesiger, P., 1999. SENSE: Sensitivity encoding for fast MRI. Magn. Reson. Med. 42, 952–962. https://doi.org/10.1002/(SICI)1522-2594(199911)42:5<952::AID-MRM16>3.0.CO;2-S

Ranson, S.W., Clark, S.L., 1959. The Anatomy of the Nervous System: Its Development and Function. Philadelphia, Saunders.

Raymond, S.B., Schaefer, P.W., 2017. Imaging Brain Collaterals: Quantification, Scoring, and Potential Significance. Top. Magn. Reson. Imaging 26, 67–75. https://doi.org/10.1097/RMR.0000000000000123

Reichenbach, J.R., Venkatesan, R., Schillinger, D.J., Kido, D.K., Haacke, E.M., 1997. Small vessels in the human brain: MR venography with deoxyhemoglobin as an intrinsic contrast agent. Radiology 204, 272–277. https://doi.org/10.1148/radiology.204.1.9205259

Rooney, W.D., Johnson, G., Li, X., Cohen, E.R., Kim, S.-G., Ugurbil, K., Springer, C.S., 2007. Magnetic field and tissue dependencies of human brain longitudinal1H2O relaxation in vivo. Magn. Reson. Med. 57, 308–318. https://doi.org/10.1002/mrm.21122

Rowbotham, G.F., Little, E., 1965. Circulations of the cerebral hemispheres. Br. J. Surg. 52, 8–21. https://doi.org/10.1002/bjs.1800520104

Rueckert, D., Glocker, B., Kainz, B., 2016. Learning clinically useful information from images: Past, present and future. Med. Image Anal., 20th anniversary of the Medical Image Analysis journal (MedIA) 33, 13–18. https://doi.org/10.1016/j.media.2016.06.009

Schmid, F., Barrett, M.J.P., Jenny, P., Weber, B., 2019. Vascular density and distribution in neocortex. NeuroImage 197, 792–805. https://doi.org/10.1016/j.neuroimage.2017.06.046

Schmitter, S., Bock, M., Johst, S., Auerbach, E.J., Uğurbil, K., Moortele, P.-F.V. de, 2012. Contrast enhancement in TOF cerebral angiography at 7 T using saturation and MT pulses under SAR constraints: Impact of VERSE and sparse pulses. Magn. Reson. Med. 68, 188–197. https://doi.org/10.1002/mrm.23226

Schulz, J., Boyacioglu, R., Norris, D.G., 2016. Multiband multislab 3D time-of-flight magnetic resonance angiography for reduced acquisition time and improved sensitivity. Magn Reson Med 75, 1662–8. https://doi.org/10.1002/mrm.25774

Shattuck, D.W., Sandor-Leahy, S.R., Schaper, K.A., Rottenberg, D.A., Leahy, R.M., 2001. Magnetic Resonance Image Tissue Classification Using a Partial Volume Model. NeuroImage 13, 856–876. https://doi.org/10.1006/nimg.2000.0730

Shu, C.Y., Sanganahalli, B.G., Coman, D., Herman, P., Hyder, F., 2016. New horizons in neurometabolic and neurovascular coupling from calibrated fMRI, in: Progress in Brain Research. Elsevier, pp. 99–122. https://doi.org/10.1016/bs.pbr.2016.02.003

Song, H.-S., Kang, C.-K., Kim, J.S., Park, C.-A., Kim, Y.-B., Lee, D.H., Kang, D.-W., Kwon, S.U., Cho, Z.-H., 2010. Assessment of Pial Branches Using 7-Tesla MRI in Cerebral Arterial Disease. Cerebrovasc. Dis. 29, 410–411. https://doi.org/10.1159/000288056

Stamm, A.C., Wright, C.L., Knopp, M.V., Schmalbrock, P., Heverhagen, J.T., 2013. Phase contrast and time-of-flight magnetic resonance angiography of the intracerebral arteries at 1.5, 3 and 7 T. Magn. Reson. Imaging 31, 545–549. https://doi.org/10.1016/j.mri.2012.10.023

Stefani, M.A., Schneider, F.L., Marrone, A.C.H., Severino, A.G., Jackowski, A.P., Wallace, M.C., 2000. Anatomic variations of anterior cerebral artery cortical branches. Clin. Anat. 13, 231–236. https://doi.org/10.1002/1098-2353(2000)13:4<231::AID-CA1>3.0.CO;2-T

Stucht, D., Danishad, K.A., Schulze, P., Godenschweger, F., Zaitsev, M., Speck, O., 2015. Highest Resolution In Vivo Human Brain MRI Using Prospective Motion Correction. PLOS ONE 10, e0133921. https://doi.org/10.1371/journal.pone.0133921

Suri, J.S., Kecheng Liu, Reden, L., Laxminarayan, S., 2002. A review on MR vascular image processing: skeleton versus nonskeleton approaches: part II. IEEE Trans. Inf. Technol. Biomed. 6, 338–350. https://doi.org/10.1109/TITB.2002.804136

Tak, S., Wang, D.J.J., Polimeni, J.R., Yan, L., Chen, J.J., 2014. Dynamic and static contributions of the cerebrovasculature to the resting-state BOLD signal. NeuroImage 84, 672–680. https://doi.org/10.1016/j.neuroimage.2013.09.057

Tang, C., Blatter, D.D., Parker, D.L., 1993. Accuracy of phase-contrast flow measurements in the presence of partial-volume effects. J. Magn. Reson. Imaging 3, 377–385. https://doi.org/10.1002/jmri.1880030213

Tetteh, G., Efremov, V., Forkert, N.D., Schneider, M., Kirschke, J., Weber, B., Zimmer, C., Piraud, M., Menze, B.H., 2020. DeepVesselNet: Vessel Segmentation, Centerline Prediction, and Bifurcation Detection in 3-D Angiographic Volumes. Front. Neurosci. 14. https://doi.org/10.3389/fnins.2020.592352

Todorov, M.I., Paetzold, J.C., Schoppe, O., Tetteh, G., Shit, S., Efremov, V., Todorov-Völgyi, K., Düring, M., Dichgans, M., Piraud, M., Menze, B., Ertürk, A., 2020. Machine learning analysis of whole mouse brain vasculature. Nat. Methods 17, 442–449. https://doi.org/10.1038/s41592-020-0792-1

Triantafyllou, C., Polimeni, J.R., Wald, L.L., 2011. Physiological noise and signal-to-noise ratio in fMRI with multi-channel array coils. NeuroImage 55, 597–606. https://doi.org/10.1016/j.neuroimage.2010.11.084

Troprès, I., Grimault, S., Vaeth, A., Grillon, E., Julien, C., Payen, J.-F., Lamalle, L., Décorps, M., 2001. Vessel size imaging. Magn. Reson. Med. 45, 397–408. https://doi.org/10.1002/1522-2594(200103)45:3<397::AID-MRM1052>3.0.CO;2-3

Tustison, N.J., Avants, B.B., Cook, P.A., Zheng, Y., Egan, A., Yushkevich, P.A., Gee, J.C., 2010. N4ITK: Improved N3 Bias Correction. IEEE Trans. Med. Imaging 29, 1310–1320. https://doi.org/10.1109/TMI.2010.2046908

Uhl, E., Lehmberg, J., Steiger, H.-J., Messmer, K., 2003. Intraoperative Detection of Early Microvasospasm in Patients with Subarachnoid Hemorrhage by Using Orthogonal Polarization Spectral Imaging. Neurosurgery 52, 1307–1317. https://doi.org/10.1227/01.NEU.0000065154.04824.9E

Uludağ, K., Blinder, P., 2018. Linking brain vascular physiology to hemodynamic response in ultra-high field MRI. NeuroImage 168, 279–295. https://doi.org/10.1016/j.neuroimage.2017.02.063

Uludağ, K., Müller-Bierl, B., Uğurbil, K., 2009. An integrative model for neuronal activity-induced signal changes for gradient and spin echo functional imaging. NeuroImage 48, 150–165. https://doi.org/10.1016/j.neuroimage.2009.05.051

van der Zwan, A., Hillen, B., Tulleken, C.A., Dujovny, M., 1993. A quantitative investigation of the variability of the major cerebral arterial territories. Stroke 24, 1951–1959. https://doi.org/10.1161/01.STR.24.12.1951

van Laar, P.J., Hendrikse, J., Golay, X., Lu, H., van Osch, M.J.P., van der Grond, J., 2006. In vivo flow territory mapping of major brain feeding arteries. NeuroImage 29, 136–144. https://doi.org/10.1016/j.neuroimage.2005.07.011

Vanzetta, I., 2005. Compartment-Resolved Imaging of Activity-Dependent Dynamics of Cortical Blood Volume and Oximetry. J. Neurosci. 25, 2233–2244. https://doi.org/10.1523/JNEUROSCI.3032-04.2005

Venkatesan, R., Haacke, E.M., 1997. Role of high resolution in magnetic resonance (MR) imaging: Applications to MR angiography, intracranial T1-weighted imaging, and image interpolation. Int. J. Imaging Syst. Technol. 8, 529–543. https://doi.org/10.1002/(SICI)1098-1098(1997)8:6<529::AID-IMA5>3.0.CO;2-C

von Morze, C., Xu, D., Purcell, D.D., Hess, C.P., Mukherjee, P., Saloner, D., Kelley, D.A.C., Vigneron, D.B., 2007. Intracranial time-of-flight MR angiography at 7T with comparison to 3T. J. Magn. Reson. Imaging 26, 900–904. https://doi.org/10.1002/jmri.21097

Wang, R.K., An, L., 2009. Doppler optical micro-angiography for volumetric imaging of vascular perfusion in vivo. Opt. Express 17, 8926–8940. https://doi.org/10.1364/OE.17.008926

Ward, P.G.D., Ferris, N.J., Raniga, P., Dowe, D.L., Ng, A.C.L., Barnes, D.G., Egan, G.F., 2018. Combining images and anatomical knowledge to improve automated vein segmentation in MRI. NeuroImage 165, 294–305. https://doi.org/10.1016/j.neuroimage.2017.10.049

Wei, L., Otsuka, T., Acuff, V., Bereczki, D., Pettigrew, K., Patlak, C., Fenstermacher, J., 1993. The Velocities of Red Cell and Plasma Flows through Parenchymal Microvessels of Rat Brain are Decreased by Pentobarbital. J. Cereb. Blood Flow Metab. 13, 487–497. https://doi.org/10.1038/jcbfm.1993.63

Wilms, G., Bosmans, H., Demaerel, Ph., Marchal, G., 2001. Magnetic resonance angiography of the intracranial vessels. Eur. J. Radiol. 38, 10–18. https://doi.org/10.1016/S0720-048X(01)00285-6

Wright, P.J., Mougin, O.E., Totman, J.J., Peters, A.M., Brookes, M.J., Coxon, R., Morris, P.E., Clemence, M., Francis, S.T., Bowtell, R.W., Gowland, P.A., 2008. Water proton T 1 measurements in brain tissue at 7, 3, and 1.5T using IR-EPI, IR-TSE, and MPRAGE: results and optimization. Magn. Reson. Mater. Phys. Biol. Med. 21, 121–130. https://doi.org/10.1007/s10334-008-0104-8

Wright, S.N., Kochunov, P., Mut, F., Bergamino, M., Brown, K.M., Mazziotta, J.C., Toga, A.W., Cebral, J.R., Ascoli, G.A., 2013. Digital reconstruction and morphometric analysis of human brain arterial vasculature from magnetic resonance angiography. NeuroImage 82, 170–181. https://doi.org/10.1016/j.neuroimage.2013.05.089

Xie, L., Kang, H., Xu, Q., Chen, M.J., Liao, Y., Thiyagarajan, M., O'Donnell, J., Christensen, D.J., Nicholson, C., Iliff, J.J., Takano, T., Deane, R., Nedergaard, M., 2013. Sleep Drives Metabolite Clearance from the Adult Brain. Science 342, 373–377. https://doi.org/10.1126/science.1241224

Xu, C., Schmidt, W.U., Villringer, K., Brunecker, P., Kiselev, V., Gall, P., Fiebach, J.B., 2011. Vessel Size Imaging Reveals Pathological Changes of Microvessel Density and Size in Acute Ischemia. J. Cereb. Blood Flow Metab. 31, 1687–1695. https://doi.org/10.1038/jcbfm.2011.38

You, J., Du, C., Volkow, N.D., Pan, Y., 2014. Optical coherence Doppler tomography for quantitative cerebral blood flow imaging. Biomed. Opt. Express 5, 3217–3230. https://doi.org/10.1364/BOE.5.003217

Yushkevich, P.A., Piven, J., Hazlett, H.C., Smith, R.G., Ho, S., Gee, J.C., Gerig, G., 2006. User-guided 3D active contour segmentation of anatomical structures: Significantly improved efficiency and reliability. NeuroImage 31, 1116–1128. https://doi.org/10.1016/j.neuroimage.2006.01.015

Zaharchuk, G., Gong, E., Wintermark, M., Rubin, D., Langlotz, C.P., 2018. Deep Learning in Neuroradiology. Am. J. Neuroradiol. 39, 1776–1784. https://doi.org/10.3174/ajnr.A5543

Zhang, Z., Deng, X., Weng, D., An, J., Zuo, Z., Wang, B., Wei, N., Zhao, J., Xue, R., 2015. Segmented TOF at 7T MRI: Technique and clinical applications. Magn. Reson. Imaging 33, 1043–1050. https://doi.org/10.1016/j.mri.2015.07.002

Zhao, J.M., Clingman, C.S., Närväinen, M.J., Kauppinen, R.A., van Zijl, P.C.M., 2007. Oxygenation and hematocrit dependence of transverse relaxation rates of blood at 3T. Magn. Reson. Med. 58, 592–597. https://doi.org/10.1002/mrm.21342

Zhu, X., Tomanek, B., Sharp, J., 2013. A pixel is an artifact: On the necessity of zero-filling in fourier imaging. Concepts Magn. Reson. Part A 42A, 32–44. https://doi.org/10.1002/cmr.a.21256